A Heterogeneous Model of the Aortic Wall Derived from Micro-Computed Tomography

Tanvi Subramanian[1], Kathleen Cao[1], Kameel Khabaz[1], Julius Kim[1], Willa Li[1], Vandana Sampathkumar[2], Narayanan Kasthuri[2], Pavel Shevchenko[3], and Luka Pocivavsek[1]

[1]Department of Surgery, University of Chicago, Chicago, IL 60637
[2]Department of Neurobiology, University of Chicago, Chicago, IL 60637
[3]Advanced Photon Source, Argonne National Laboratory, Lemont, IL 60439

The aorta is the largest artery in the body, and it is composed of three layers: intima, media, and externa/adventitia. The media is mostly composed of collagen and elastin, and collagen is the dominant contributor to the strength and structural stability of the aorta. Aortic diseases such as aneurysms and dissections lead to distortion of the aortic wall. We aim to demonstrate local aortic tissue biodynamics via collagen and elastin fiber remodeling in murine aorta at varying distension using micro-computed tomography (microCT). Ten week-old C57BL/6 mice were injected via tail vein with in-vivo collagen hybridizing peptide, which reforms the triple-helix structure of denatured collagen. Careful dissection and removal of the thoraco-abdominal aorta was performed, which was pressurized with formalin at varying distensions. Samples were then prepared via heavy-metal staining, and fixed in epoxy resin. The samples were imaged at the microCT scanner at University of Chicago and beamline 2-BM-B at the Advanced Photon Source to obtain micron and sub-micron resolution images and thus provide multi-level views of the tissue. Clear visualization of distinct collagen and elastin layers was observed with microCT and illustrate the effect on individual collagen and elastin fiber organization created by over-distension and shear-stress on the aorta. Models were created for local regions of the aorta via segmentation, smoothing, and meshing, and these models served as inputs for finite element analysis. Stress-strain relationships were extracted from simulations where velocity-based forces in either the circumferential or longitudinal direction were applied. We ultimately aim to produce a multi-scale imaging model of aortic failure with our methods.

This research used resources of the Advanced Photon Source, a U.S. Department of Energy (DOE) Office of Science user facility operated for the DOE Office of Science by Argonne National Laboratory under Contract No. DE-AC02-06CH11357.

A Heterogeneous Model of the Aortic Wall Derived from Micro-Computed Tomography

Tanvi Subramanian[1], Kathleen Cao[1], Kameel Khabaz[1], Julius Kim[1], Willa Li[1], Vandana Sampathkumar[2], Narayanan Kasthuri[2], Pavel Shevchenko[3], and Luka Pocivavsek[1]

[1]Department of Surgery, University of Chicago, [2]Department of Neurobiology, University of Chicago, [3]Advanced Photon Source, Argonne National Laboratory

Background and Project Aim

- The aorta is the largest artery in the body composed of 3 layers: intima, media, and adventitia
- The media is mostly composed of collagen and elastin
  - Collagen is dominant contributor to aortic strength and stability
- Aortic aneurysm: 9th leading cause of death in U.S., leading to 10,000 deaths annually
- Pathogenesis of aneurysmal disease is dependent on collagen and elastin turnover
- Aneurysm rupture results from mechanical failure: peak wall stress exceeds local tissue strength
- Exemplified in Marfan's syndrome; markedly altered collagen architecture leads to incoherent mechanical network
- Current practice: aortic segmentation from computed tomography (CT) imaging undergoes finite element analysis (FEA) to test real-world stresses
  - This method lacks the ability to study **local** aortic responses to the same stresses
- We aim to develop a model of collagen and elastin behavior in murine aorta at different geometric points by utilizing high resolution micro-CT imaging, and segmenting these individual layers throughout the entire aorta
- This will allow us to study how the aorta deforms to blood pressure the local level

Methods

- Aortas from 10-wk old C57/BL6 mice were dissected out and pressurized with formalin to varying distensions. These samples were prepared via extensive heavy-metal staining process and fixed in epoxy resin.
  - Some samples were injected with in vivo collagen-hybridizing peptide (CHP) via tail vein
- Sub-micron imaging was obtained at the 2-BM-B beamline (Advanced Photon Source, Argonne National Laboratory), providing fiber-localized imaging of the same samples.

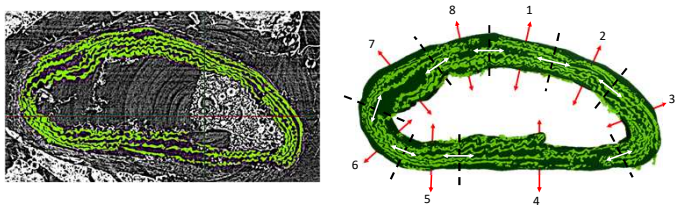

- Segmentation (Simpleware ScanIP, Synopsys) of elastin (light green) from microCT images was performed and interstitial regions defined as collagen (dark green)
- The segmentation was smoothed and meshed and contained over 12 million elements
- The aorta ring was divided into 8 sections containing 1-2 millions for FEA (Abaqus, Dassault Systemes) and used material properties from the literature (Pocivavsek & Milner JVS 2020):
  - Density: 1.12 x 10^{-6} kg/mm^3; elastin: C10=0.001, D1=50; collagen (1X): C10=0.001, D1=50; and collagen (100X): C10=0.1, D1=0.5
  - To study tissue response to uniaxial pressurization, the sections were subjected to velocity-based circumferential (red arrows) and longitudinal loading (white arrows)
  - Stress (σ)-strain (ϵ) analysis on representative areas in each section to determine the Young's modulus, E, from linear fits of the stress-strain curves.

$$\sigma = E\epsilon$$

Results: MicroCT Images of Murine Aortas from 2-BM

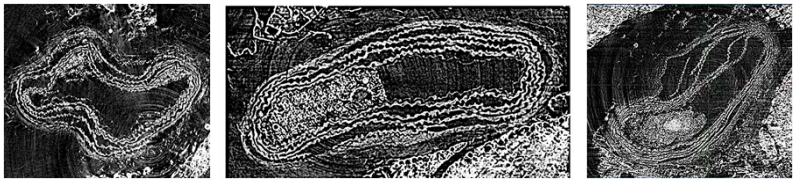

Localized view of aorta: Sub-micron level CT images demonstrating elastin layer of aortic wall, in order of increasing distension from left to right

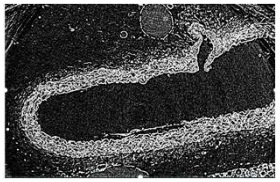

Addition of CHP confirms presence of collagen in between elastin layers

Results: FEA Simulations and Stress-Strain Curves

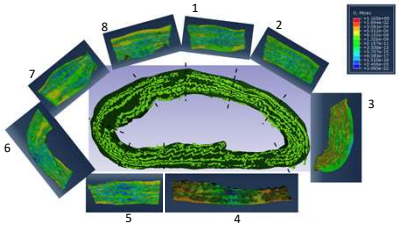

Representative images at the end of the simulations depicting the von Mises stress in each aortic wall section. Shown is the system where collagen is 100X stiffer than elastin subjected to longitudinal pressurization.

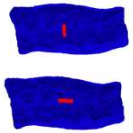

Representative images of area samples selected for stress-strain analysis (red). Shown is Section 1 where collagen is 100X stiffer than elastin subjected to longitudinal pressurization.

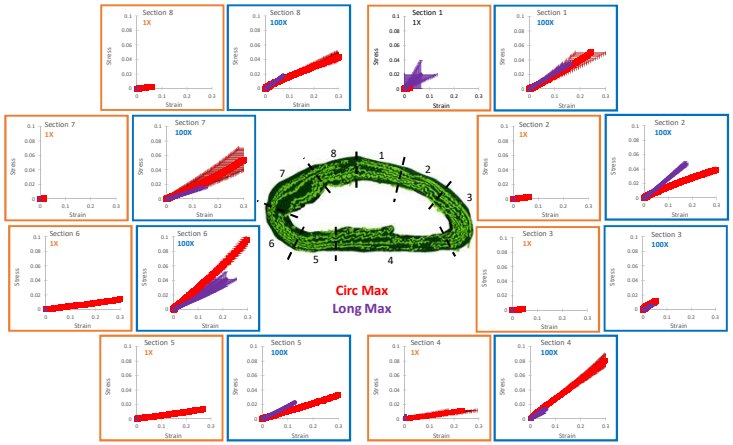

Results: Young's Modulus, E

Section	E, Circ Max (MPa)		E, Long Max (MPa)	
	1X	100X	1X	100X
1	43	196	296*	216
2	44	129	42	272
3	43	234	42	157
4	48	283	42	254
5	47	123	42	176
6	45	406	39	187
7	43	176	42	115
8	44	147	40	251
average	44	220	73*	203
variance	0.003	9	81	29
% variance/average	0.01%	4.30%	11.07%	1.44%

Preliminary Conclusions and Next Steps

- Initial development of heterogeneous murine aortic model based on microCT imaging at fiber-localized levels but further validation and tests are needed
  - For 1X systems, the expected Young's modulus is 6 Mpa given the inputs but our results show E values 7 times greater than expected. This may be due to the geometry of each section but further investigation is needed.
  - It is also unclear why some of the strains are very low
- Results show that as the stiffness of the collagen increases (1X to 100X), the pressure gradient is well-distributed along the length of the elastin fibers
- This novel method will allow for development of complex aortic fracture model to study aortic pathologies
- In general, the maximum stresses due to circumferential loading is the dominant force
- The stresses are more pronounced when the material properties between collagen and elastin are different (100X has greater stresses than 1X) thereby providing evidence that local structure is important in aortic biomechanics
- Future experiments include using *FBN1* (Marfan's phenotype) mice to compare diseased aortas against this healthy murine mice data

Acknowledgements

This research used resources of the Advanced Photon Source, a U.S. Department of Energy (DOE) Office of Science user facility operated for the DOE Office of Science by Argonne National Laboratory under Contract No. DE-AC02-06CH11357.

Geometry of Life and Disease: The Role of Large-field Submicron Resolution Tissue Tomography

Keith C. Cheng[1, 2] and Patrick J. La Riviere[3]

[1]Department of Pathology and Jake Gittlen Laboratories for Cancer Research, Penn State College of Medicine, Hershey, PA 17036
[2]Institute of Computational and Data Sciences, Pennsylvania State University, University Park, PA 16802
[3]Department of Radiology, University of Chicago, Chicago, IL 60637

All multicellular organisms are comprised of cells and extracellular components that possess theoretically quantifiable, three-dimensional features (size, shape, volume, texture) and relationships (density, arrangements, proportions) organized into tissues, organs, and organ systems. Physiological and disease states are marked by physical change on the micron scale that in turn requires submicron pixel resolutions. To digitally define the geometry of life, we need to be able to image all cell types, analogous to what is done in histology, over fields-of-view (FOV) of millimeters to centimeters to obtain organ context. To achieve this, we have pursued centimeter scale 3-dimensional imaging at isotropic submicron voxel resolutions.

We have developed large-field, high resolution instrumentation in conjunction with fixation and metal-staining approaches over a decade of collaboration with biologists, x-ray physicists, and engineers, yielding a tissue tomography that we call *histotomography* [1]. Since we need FOV larger than the less than 2 mm provided by traditional microscope lenses, we prototyped centimeter scale field-of-view lenses paired with large chip array digital cameras to yield submicron pixel resolution over 5 to 12 mm [2]). This instrumentation will increase our understanding of the diversity of life, biological and gene function, development, and disease [3] and be applicable to more powerful toxicology, and biomedical diagnostics. We will discuss scientific gaps that remain, potential directions, and review in particular the role of synchrotron tomographic beamlines in creating the infrastructure for community-based characterization of the geometry of life and disease, and development of the field of computational phenomics.

We thank Steve Yuxin Wang for large-field, high-resolution imaging system design and prototyping, and Francesco DeCarlo, Xianghui Xiao, Alan Kastergren, and Dula Parkinson for guidance in planning the role of the DOE in computational phenomics.

[1] Ding Y, et al., La Rivière PJ, and Cheng KC. Computational 3D histological phenotyping of whole zebrafish by x-ray histotomography. *eLife*. 2019 May 7;8:e44898.
[2] Yakovlev MA, et al., La Riviere PJ, and Cheng KC (2022) A wide-field micro-computed tomography detector: micron resolution at half-centimetre scale. *Journal of Synchrotron Radiation*, 29(Pt 2), 505–514. https://doi.org/10.1107/S160057752101287X. PMID: 35254315.
[3] Cheng KC et al. (2022) Promoting validation and cross-phylogenetic integration in model organism research. *Dis Model Mech.* Sep 1;15(9): dmm049600. doi: 10.1242/dmm.049600. Epub 2022 Sep 20. PMID: 36125045.

Geometry of Life and Disease (*GOLD*): A Systems Approach to Broadening the Societal Benefits of Large-field Submicron Tissue Tomography

Keith C. Cheng (Pennsylvania State University) and Patrick La Riviere (University of Chicago)

Abstract

Towards the goal of collaborative global illumination of phenotype caused by change in genes, environment, and disease, we are targeting the quantitative and reproducible phenotyping of organisms and tissues utilizing a diagnostic foundation of medicine, "histopathology" (phenotyping across cell and tissue types). We are taking a systems approach to collaboratively create a quantitative, and high-throughput 3D histopathology for phenomic studies of model organisms, limited only by the laws of physics. To apply these principles to model organisms and human issues, "pan-cellular" imaging (across all cell the tissue types) at high resolution will enable higher dimensions of characterization of tissue phenotypes than presently possible. We want to apply the advantages of histology in 3D for the high-throughput and quantitative needs of phenomics to make volumetric measurements of organs and of cells and their relationships. We have used fixation and metal-staining to create pan-cellular 3D reconstructions of whole organisms. Next steps in this highly collaborative effort include planning the installation and community use of large-field, submicron tissue tomography instrumentation at synchrotrons, piloting broad user availability, enabling web-based 3D visualization tools, and demonstrating the potential of cell-specific and whole-organism phenotyping.

Biomedical Foundations for *GOLD*

Distinguishing between cellular mechanism of the small eye phenotype of *a* zebrafish mutant requires submicron pixel resolution. Stereomicroscopy (*left*), a standard morphology screening tool, shows *hht* eyes to be smaller than wild-type, but can not distinguish between lack of formation and cell death (apoptosis). In contrast, the submicron pixel size of histology (*below*) allows us to visualize nuclear debris whose fragments are of single micron dimension. Thus, the small eyes of *hht* are associated with apoptosis, disorder and debris, not lack of development.

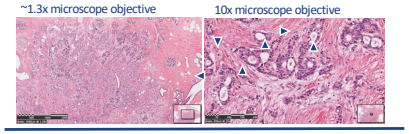

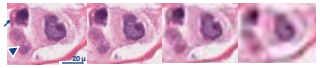

Microscope Objective	40x	20x	10x	5x
Pixels (µ x µ)	0.25	0.5	1	2
Chromosomes visible?	Yes	Yes	Barely	No
Golgi (*G*) visible?	Yes	Yes	Barely	No

Histopathology: submicron pixel resolution

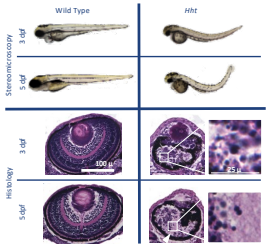

(Left) **The small eye phenotype of *a zebrafish polymerase* mutant illustrates the importance of submicron pixel resolution.**. Stereomicroscopy, a standard morphology screening tool, shows *hht* eyes are smaller than the corresponding wt. Histology reveals cellular mechanism: apoptosis of cells, associated with cellular disorder and nuclear debris.

(Below) **Histology-based phenotyping of stained tissues is more sensitive than live fish stereomicroscopy live fish.** A whole-animal histologic screen of stereomicroscopy-identified mutants revealed unexpected pleiotropy, cellular "atypia" characteristic of cancer progression, and 3.3x higher sensitivity for identifying phenotypes.

Greater resolution reveals that pleiotropy is common

Distinguishing alternative cellular mechanism underlying phenotypes such as small eye phenotype in zebrafish requires submicron pixels. We showed that many phenotypes readily detectable by histology cannot be seen in a dissecting microscope. Overall, <1/3 of histological phenotypes are detectable by dissecting microscope.

Organ:		Kidney	Integu-Ment	Pancreas	Fin	Brain	Pharynx	Eye	Liver	Gut	TOTAL
# Phenotypes In 97 mutants @ 5 dpf	Stereo (~5 µ pixels)	0	0	1	4	8	21	72	52	58	**216**
	Histology (< 0.5 µ pixels)	81	48	67	81	87	77	93	79	91	**704**
% Histologic phenotypes detected by stereomicroscopy		0	0	~1	5	59	27	77	66	64	**31**

(Analysis by G. Thomas, B. Canada, K. Cheng)

Histotomography

Developing *histotomography involved* combining pan-cellular staining, microCT, and variable-thickness visualization to characterize 3D cellular features. ~6.5 x 0.6 mm zebrafish larvae stained with phosphotungstic acid and imaged at 2BM.

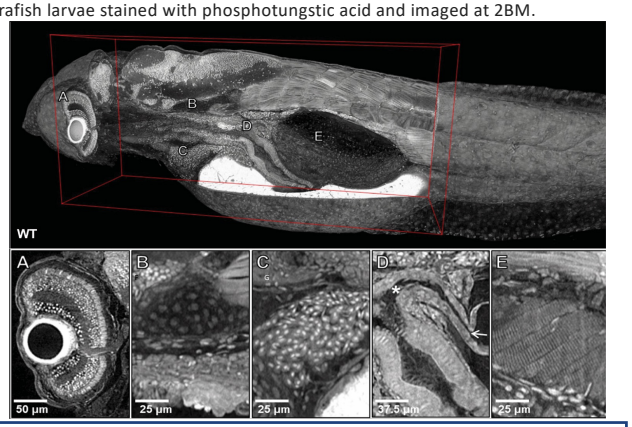

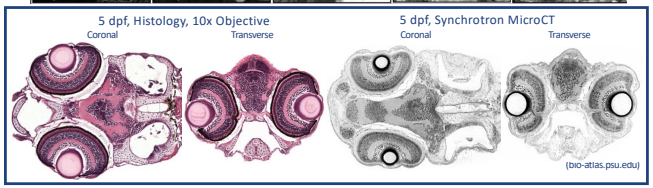

Scale and resolution

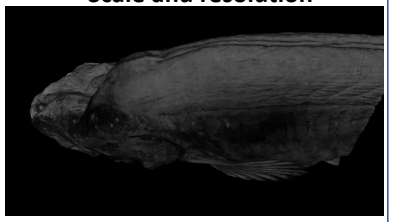

Movie of a whole juvenile zebrafish illustrating the power of visualizing mm scale structures. Imaged at 2-BM at at 1.4 µ isotropic resolution, now available at 0.5 µ.

Centimeter scale FOVs are needed for whole-organism phenotyping of small model systems and tissue specimens from larger organisms including humans. This required custom large-FOV optics based on photolithography lenses and 150 MP chips. (See Yakovlev et al. poster)

GOLD Timeline

- **2010** — Compare Commercial with Synchrotron MicroCT
- **2018** — Establish synchrotron histotomography
- **2022** — Develop Instrumentation with submicron voxel resolution and centimeter scale FOV
- **2025** — Pilot user access to Synchrotron histotomography
  - Web-based 3D visualization
  - Organ and cell segmentation
- **2026** — Finalize user access to synchrotron histotomography for the Geometry of Life and Disease Consortium
- **2026** — Global Imaging and Analysis
- **2026-** — **IMPACTS**
  - Tissue Diagnostics
  - Drug development
  - Environmental Toxicology
  - Define Phenotypic Signatures

Geometry of Life: Organs

Histotomography allows accurate full resolution labels scaled from sparse segmentation. *A*: original reconstruction down-sampled to quarter resolution. *B:* ultra sparse subset of slices are labeled for the researchers' ROI. *C:* informed interpolation using Biomedisa. *D:* resulting 3D label set is then upscaled to generate a full resolution label mask and smaller sub-volume file, from cell segmentations can be done.

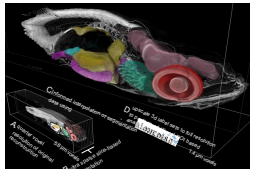

Geometry of Life: Cells

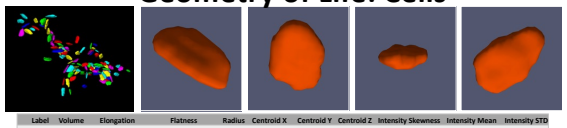

Label	Volume	Elongation	Flatness	Radius	Centroid X	Centroid Y	Centroid Z	Intensity Skewness	Intensity Mean	Intensity STD
1	485	2.044755569	1.978420507	4.873987112	427.1113402	669.1113402	675.187629	1.546299253	33396.57732	101.3327343
2	465	1.23269107	2.348048489	4.806048117	426.2408602	624.1827957	681.503226	1.241627797	252.4215054	34.66630007
3	508	1.889382837	2.336467484	4.948846156	433.5334646	610.1122047	682.86811	0.943603433	504.1181102	72.77439285
4	623	1.719233294	2.604383163	5.298258527	395.6902087	639.3226324	683.394864	0.951936665	33405.43178	112.5925189
5	220	1.288351598	3.494497857	3.744938504	418.1727273	653.5090909	685.013636	0.812219319	530.3636364	74.56378193
6	497	1.428258665	2.047959604	4.913857898	421.3541247	691.9517103	688.573441	1.449939229	33356.32998	93.44831981
7	492	1.549733517	2.485615065	4.897323931	417.4979675	639.1097561	692.310976	0.784399081	33139.48171	66.50551384
8	214	2.303320261	2.113738077	3.710579333	398.7429907	586.9719626	723.551402	0.695995061	32925.13084	19.58493438
9	240	1.680079762	2.490758963	3.855146421	406.2791667	599.4833333	731.275	0.61620881	32930.3875	20.56695999
10	203	1.765318617	2.506025627	3.64588089	380.1182266	577.4778325	743.226601	0.871425905	308.8965517	34.73583675
50	164	1.983034299	1.968215806	3.395614262	315.1203317	553.2865854	829.829268	1.043375494	303.3658537	41.01193386
AVG:	340.4	1.924	2.396	4.224	394.564	591.511	769.884	0.73397	15709.97	2335.181

Ke Liang, M. Yakovlev, S. Huang, and K. Cheng

Histotomography enables volumetric measurements of thousands of cells. Supervised machine learning was used to create automated blood cell segmentation from whole larval zebrafish histotomograms. Geometric parameters are based on ellipsoid models.

Histotomography-enabled Phenomics Overview

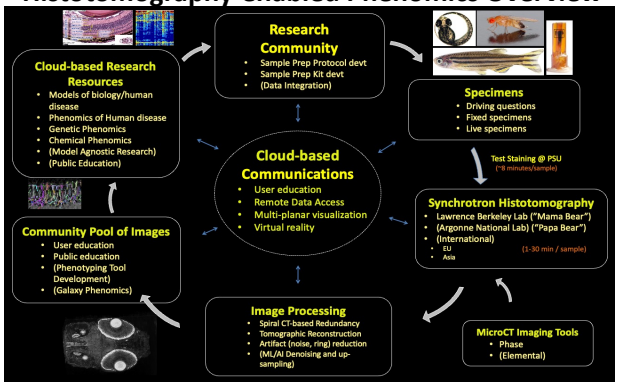

"There is no Planet B"

Too Many:
- Genes
- Chemicals
- Diseases
- cause combinations
- Phenotype combinations

Imagine:
Whole-organism phenotyping
- Daphnia
- Drosophila
- Zebrafish
- Mouse
- Other

Chemical Phenomics
- Drug Phase 1
- Environmental Toxicology

Tissue Diagnostics
- Human
- Model systems

Genetic Phenomics
- All functions
- All genes

Histotomography Demo

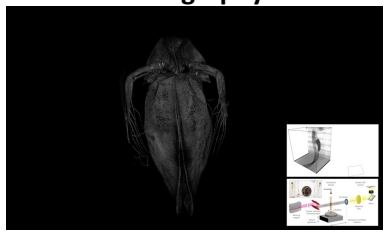

References:

1. Ding Y, et al., La Rivière PJ, and Cheng KC. Computational 3D histological phenotyping of whole zebrafish by X-ray histotomography. *eLife*. 2019 May 7;8:e44898.
2. Yakovlev MA, et al., La Riviere PJ, and Cheng KC (2022) A wide-field micro-computed tomography detector: micron resolution at half-centimetre scale. *Journal of Synchrotron Radiation*, 29(Pt 2), 505–514.
3. Cheng KC et al. (2022) Promoting validation and cross-phylogenetic integration in model organism research. *Dis Model Mech*. Sep 1;15(9): dmm049600.

Contributors: S Katz, M Yakovlev, DJ Vanselow, MS Ngu, CR Zaino, SR Katz, Y Ding, AY Lin, P Vargas, J Copper, R Saint-Fort, A Sugarman, SY Wang, D Mandrell, KC Ang, D Northover, K Liang, A Adesiha, J Liechty, S Huang, **F De Carlo**, **X Xiao**, **D Parkinson**, **A Kastengren** (Bold: DOE)

Metals in Brain *vs* Neurodegenerative Disorders

Pavani Devabathini[1] and Yulia Pushkar[1]

[1]Department of Physics and Astronomy, Purdue University, West Lafayette, IN 47907

Disruption in homeostasis of metals present inside the brain are implicated in the etiologies of several neurodegenerative disorders such as Parkinson's disease, Alzheimer's disease [1]. Hence, acquiring knowledge on spatial distribution and concentration of these metals within the brain paves a way to better understand the mechanisms of these diseases. The techniques that have been utilized for decades such as imaging followed by immunohistochemical staining of tissue, auto-metallographic techniques, mass spectroscopy either alter the concentration of metals from tissue fixation or lack spatial resolution [2, 3].

Here we use synchrotron x-ray fluorescence spectroscopy on unfixed tissue sections to measure concentrations of multiple metals of interest both at tissue and cellular level within the brains. Our results indicate that mercury (Hg), a highly toxic heavy metal is localized within the choroid plexus and lateral cerebral ventricular wall of our animal model (wildtype small Indian mongoose). We were further able to locate that astrocytes preferentially accumulate this metal, this metal colocalizes almost to a full extent with selenium, indicating a Se-based detoxification mechanism of Hg. We were also able to localize manganese (Mn) to purkinje cellular layer in the cerebellum of SLC39A14 (a manganese transporter gene) -knocked out model of mice thereby reporting that in addition to the previously reported periventricular zone, cells from cerebellum play a major role in the etiology of Parkinson's disease.

[1] S. Pfaender, A.M. Grabrucker, Characterization of biometal profiles in neurological disorders, Metallomics 6(5) (2014) 960-77.
[2] S. Horai, Y. Nakashima, K. Nawada, I. Watanabe, T. Kunisue, S. Abe, F. Yamada, R. Sugihara, Trace element concentrations in the small Indian mongoose (Herpestes auropunctatus) from Hawaii, USA, Ecological Indicators 91 (2018) 92-104.
[3] G. Danscher, Applications of autometallography to heavy metal toxicology, Pharmacol Toxicol 68(6) (1991) 414-23.

Metals in Brain Vs Neurodegenerative Disorders

Pavani Devabathini[a], Darrell Fischer[a], Qingyang Li[a], Yulia Pushkar[a]
[a] Department of Physics and Astronomy. Purdue University

Research Question #1

Will Mn concentration be affected in the Purkinje Cellular Layer (PCL) in the cerebellar cortex of SLC39A14 –KO model mice?

Photomicrograph of a silver-stained section of cerebellum[1]

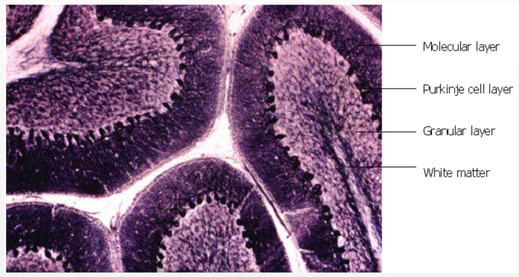

Background

- SLC39A14 encodes a member of divalent metal transporters that mediate the cellular uptake of Mn, Zn, and Cd.
- Loss of function mutations of SLC39A14 is reported in childhood-onset manganese induced dystonia parkinsonism
- Despite Mn being an essential trace metal, chronic exposure to high levels of Mn is known to cause a condition called manganism.
- Manganism mimics the symptoms of Parkinson's disease.
- Motor capabilities of individuals are affected in Parkinson's disease.
- Purkinje cells are necessary for well-coordinated motor activities

Methodology

Optical set up at 9-ID, BNP, APS, Argonne National Laboratory[2]

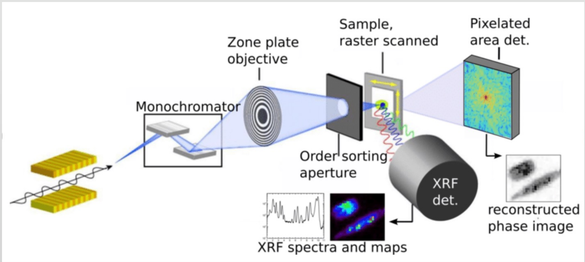

- Thickness of sample for tissue imaging is 30 micrometers.
- Thickness of sample for cellular/sub-cellular imaging is 10 micrometers.
- Energy of x-ray beam stood at 10.5 keV for research project #1
- Energy of x-ray beam stood at 15.7 keV(tissue level), 12.7 keV (cellular level) for research project #2

Results

Detector spectra obtained from PCL of SLC39A14 – knocked out (KO) mice and wildtype mice shows significantly more Mn in knocked out model.

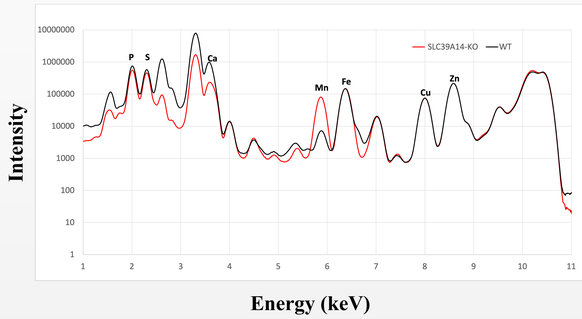

Elemental XRF distribution in cerebellum shows significantly more Mn in PCL of SLC39A14 knocked out model mice

SLC39A14 – KO model **Wild-type model.**

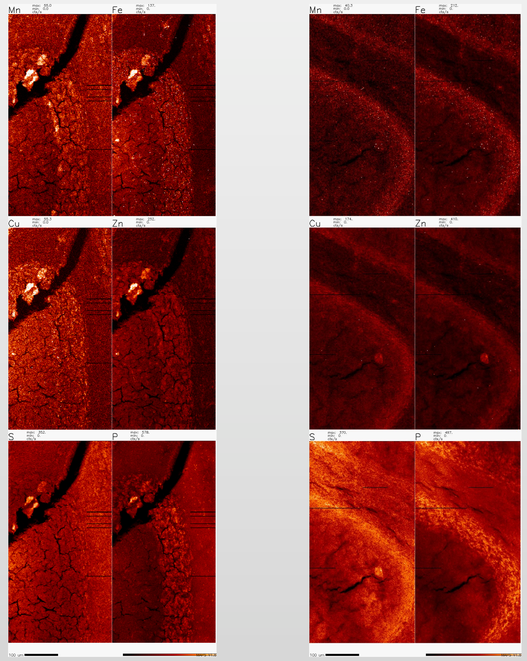

Conclusions and Future Directions

- The concentration of Mn increases by 10-fold in knocked out model mice.
- Localize Mn-aggregates at a sub-cellular level

Research Question #2

- What does the tissue specific distribution of Mercury (Hg) look like in the brain of small Indian mongoose?
- At tissue-level, where is major amount of Hg concentrated in this brain?
- Which cellular or sub-cellular components is Hg localized to?

Background

- Minamata disease is a result of Hg –poisoning.
- Hg is an ubiquitous element and is present in high concentrations in marine biota[3]
- Marine mammals are known to possess an Hg- detoxification mechanism
- Multiple hypotheses for the detoxification mechanism exist arguing HgSe to be the end species
- Small Indian mongoose has been found to possess high Hg concentrations in the liver.[4]
- Choroid plexus floats in the cerebrospinal fluid present in the cerebral ventricular voids and protects brain against toxic metals.

Results

Hg is found distributed throughout the brain tissue

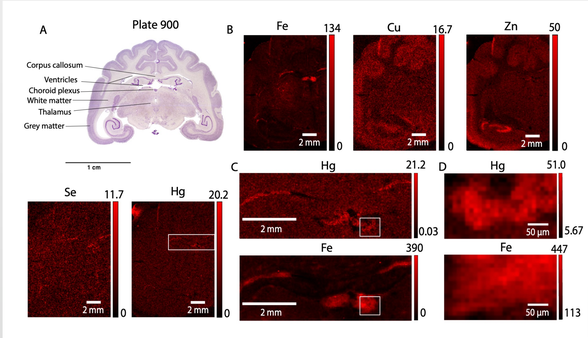

Majority of Hg is found in the choroid plexus and cerebral lateral ventricular wall with a molar ratio of [Hg]:[Se] =1.5 - 3.0

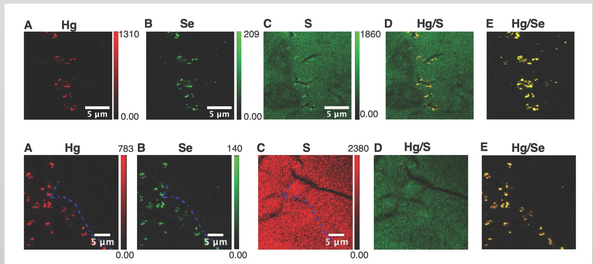

All units are in micrograms/gram of wet tissue weight

Hg is localized to the astrocytes lining the cerebral ventricular wall

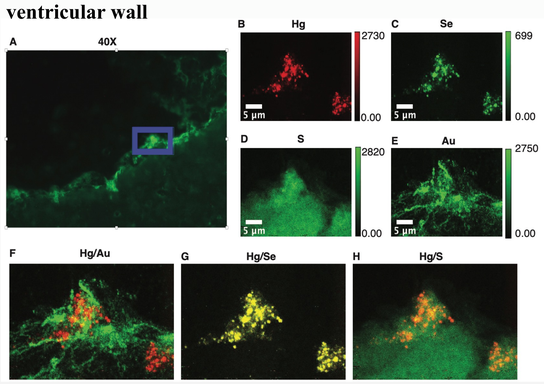

Hg is not present inside the lysosomes within the cells.

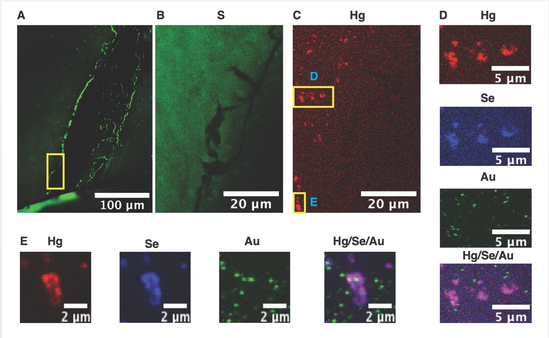

Conclusions and Future Directions

- The end species in this animal model is not HgSe, as molar Hg:Se is 1:1 for these nanoparticulates.
- Chemical form of the aggregates using XANES and EXAFS.

References

1.http://staff.um.edu.mt/acus1/Cerebellum.htm
2.S. Chen, et al., "Simultaneous x-ray nano-ptychographic and fluorescence microscopy at the bionanoprobe," Proc. SPIE 9592, X-Ray Nanoimaging: Instruments and Methods II, 95920I (18 September 2015).
3.R. Dietz, et al., A risk assessment review of mercury exposure in Arctic marine and terrestrial mammals, Sci Total Environ 829 (2022) 154445.
4.S. Horai, et al., Trace element concentrations in the small Indian mongoose (Herpestes auropunctatus) from Hawaii, USA, Ecological Indicators 91 (2018) 92-104

Acknowledgements

We express our sincere gratitude to our collaborators Dr. Sawako Horai, Prof. Tomas R.Guilarte, Alexander N. Rodichkin in addition to the beamline scientists Dr. Si Chen, Dr. Olga Antipova at Argonne National Laboratory and Dr. Yong Chu, Dr. Xiaojing Huang, Dr. Ajith Pattamattel at Brookhaven National Laboratory.

Improvements in Reconstruction Pipelines to Facilitate 3D Histological Analysis of COVID-19 Lung Samples

David Northover[1,2], Maksim Yakovlev[1,2,3], Carolyn Zaino[1,2], Daniel Vanselow[1], Mee Siing Ngu[1,2], Khai Chung Ang[1,2], Kris Ylaya[4], Stephen Hewitt[4], and Keith C. Cheng[1,2]

[1]Department of Pathology, Penn State College of Medicine, Hershey, PA 17033
[2]The Jake Gittlen Laboratories for Cancer Research, Penn State College of Medicine, Hershey, PA 17033
[3]Biomedical Sciences PhD Program, Penn State College of Medicine, Hershey, PA 17033
[4]Laboratory of Pathology, Center for Cancer Research, National Cancer Institute, National Institutes of Health, Bethesda, MD 20892

Two-dimensional histological analysis is limited by the sectioning artifacts from slicing tissue at sufficient thickness to retain stability. High-resolution wide-field micro-CT imaging overcomes this challenge and gains isotropic resolution across all axes, enabling 3D histological analysis that allows accurate characterization of volume, shape and distribution of small structures and cells in biological tissue. However, such large images can present technical challenges for reconstruction and analysis due to the high computational demands, particularly when considering methods to remove scanning artifacts and improve signal to noise ratio.

Fixed, embedded, and PTA-stained lung samples from 3 individuals deceased from COVID-19 at varying levels of disease progression were scanned at Argonne National Labs at 0.7 µm resolution and 10 mm x 7mm field of view, yielding 1.25 TB section scans totaling 2.5 to 8.75 TB per sample. Improvements in memory handling and computational efficiency of several steps in the overall reconstruction process allowed significant improvements in reconstruction time and hardware usage. Three-dimensional histology for these samples is presented alongside 2D histological data of adjacent tissue for co-registration. Future approaches to characterizing the pathology along with the advantages of 3D histology are presented.

The authors are very grateful to Dr. Alan Kastengren at 7BM and to Alex Deriy, Dr. Viktor Nikitin, Pavel Shevchenko, and Dr. Francesco de Carlo at 2BM of the Argonne National Laboratory Advanced Photon Source for their crucial assistance in temporarily integrating our detector with their hutch, data acquisition, and other intellectual contributions to the performed work. Dr. Steve Y Wang of Mobile Imaging Innovations, Inc provided essential work on the design and development of the detector hardware and Dr. Patrick J. La Riviere of the University of Chicago provided key guidance.

Improvements in Reconstruction Pipelines to Facilitate 3D Histological Analysis of COVID-19 Tissue Samples

David Northover[1,2], Maksim Yakovlev[1,2,3], Carolyn Zaino[1,2], Daniel Vanselow[1], Mee Siing Ngu[1,2], Khai Chung Ang[1,2], Kris Ylaya[4], Zissis Chroneos[1], Stephen Hewitt[4], Keith Cheng[1,2]

[1] Department of Pathology, Penn State College of Medicine, Hershey, Pennsylvania, USA; [2] The Jake Gittlen Laboratories for Cancer Research, Penn State College of Medicine, Hershey, Pennsylvania, USA; [3]Biomedical Sciences PhD Program, Penn State College of Medicine, Hershey, Pennsylvania, USA; [4] Laboratory of Pathology, Center for Cancer Research, National Cancer Institute, NIH, Bethesda, MD, USA

ABSTRACT

2D histological analysis is limited by the sectioning artifacts from slicing tissue at sufficient thickness to retain stability. High-resolution wide-field Micro-CT imaging circumvents this and gains isotropic resolution across all axes, enabling 3D histological analysis that allows accurate characterization of volume, shape and distribution of small structures in biological tissue. However, such large images can present technical challenges for reconstruction and analysis due to the high computational demands, particularly when considering methods to remove scanning artifacts and improve signal to noise ratio.

Fixed, embedded, and PTA-stained lung samples from 3 individuals deceased from COVID-19 at varying levels of disease progression were scanned at Argonne National Labs at 0.7 µm resolution and 10 mm x 7mm field of view, yielding 1.25 TB section scans totaling 2.5 to 8.75 TB per sample. Improvements in memory handling and computational efficiency of several steps in the overall reconstruction process allowed significant improvements in reconstruction time and hardware usage. 3D histology for these samples is presented alongside 2D histological data for adjacent tissue data for co-registration, and future approaches to characterizing the pathology and its relation to disease progression are presented along with the advantages presented by 3D histology.

OBJECTIVES

1. Reduce memory usage to enable broader parallelization on both high-powered and low-powered hardware.
2. Target key performance bottlenecks to allow better throughput of data reconstruction.
3. Identify key cell types for tracking cell and tissue damage arising from COVID-19 in both conventional and 3D, Micro-CT based histology.
4. Use computational categorization and characterization of cells in both 3D and conventional histology, both to fully track the effect of COVID-19 and examine the benefits of using 3D histology approaches in practice.

MATERIALS AND METHODS

2 post-mortem samples for each of 3 individuals deceased from COVID-19 at medium or late stage were obtained from the NIH. Samples were stained with PTA and embedded in JB4+ as per standard protocol[2]. These samples were scanned at Argonne National Laboratories Labs at 0.7 µm resolution and 10 mm x 7mm field of view using a custom scintillator setup and a VP601MX camera[1].

Mouse lung and trachea samples (used in benchmarking, not shown here) were obtained from Zissis Chroneos. Samples were stained with PTA and embedded in JB4+ as per standard protocol[2], then scanned at Lawrence Berkeley National Laboratory at 0.5 µm resolution and a 5.8 mm x 4.5mm field of view with a VP101mx camera[1].

Samples were reconstructed on a High Performance Cluster system based at Hershey Medical Center. Runs (both benchmarked and shown reconstructed) were run on either 4 (88 thread/process) or 2 (44 thread/process) dense nodes with 88 cpu thread capacity and 1.5T memory.

Optimizations were performed by a mix of refactoring existing implementations (tomopy[3,4,5] and algotom[6]) and converting memory usage to a shared memory approach to avoid the overhead of excess data copies and the inefficiencies around data dispatching during python multiprocessing.

Additionally, modifications were made to the phase retrieval algorithm to align more closely with the original intended approach[4], based on filed tomopy issues.

RESULTS

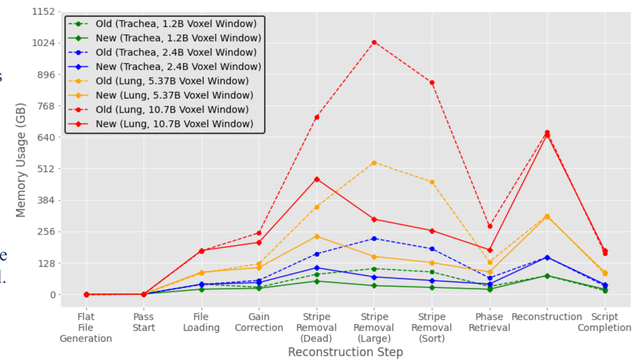

Figure 1 Memory usage at each reconstruction step. Memory usage (GB) before and after our optimization is compared when reconstructing a mouse trachea (97.26 billion voxels) and a mouse lung (515.76 billion voxels). Our approaches reduced total memory usage, specifically during gain correction, stripe removal, and phase retrieval. Notably, usage was reduced by 66-70% during Stripe Removal (Large), the most memory intensive step.

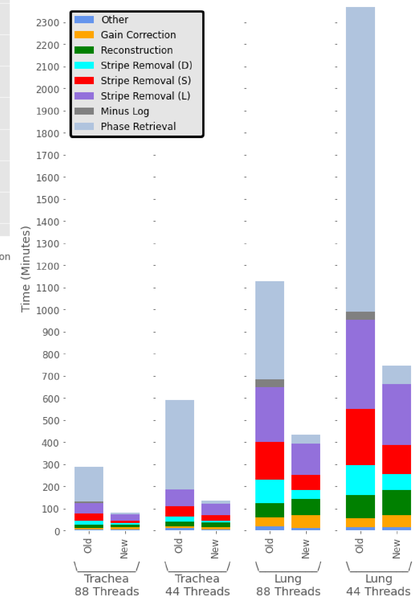

Figure 2 (Right) Optimization reduced reconstruction time. Reconstruction time of mouse trachea (97.26 billion voxels) and mouse lung (515.76 billion voxels) is compared. Minor steps are binned in "Other." Optimizations have reduced phase retrieval time by > 90% and total stripe removal time by > 45%. Lower thread count approaches are longer in duration but can be run individually on smaller nodes to adapt to lower hardware requirements or doubled on larger nodes for faster reconstruction.

Figure 3 (Below) Histology and MicroCT of Adjacent COVID Tissue. A and B are hematoxylin and eosin stained histology at 10x; and C and D PTA-stained MicroCT, 0.7 µm resolution (zoomed out by x3).

A and **C** are adjacent post-mortem samples from an individual deceased from medium-stage COVID-19.

B and **D** are adjacent post-mortem samples from an individual deceased from late-stage COVID-19.

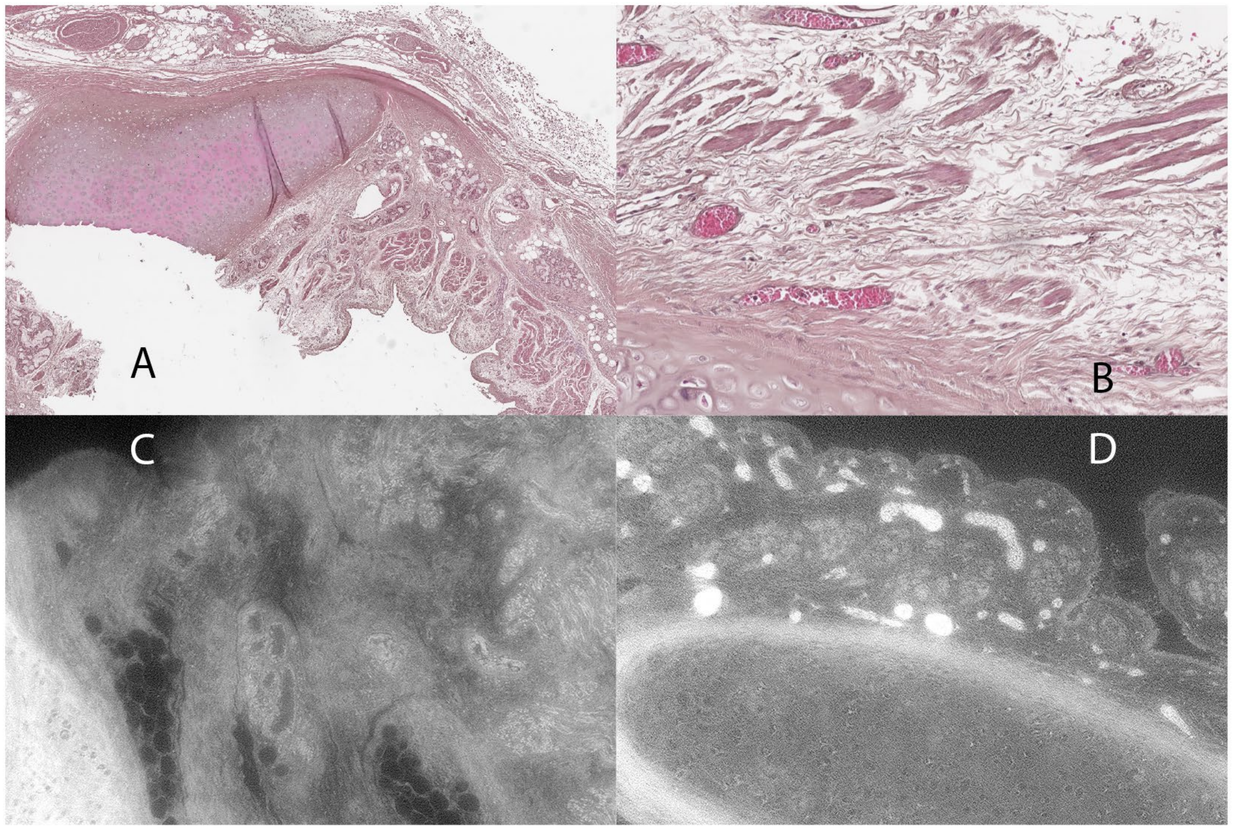

NEXT STEPS

The largest computational targets remaining focus around two issues. First, the performance and memory usage of existing median filter algorithms, which are limited to sort based algorithms as the existing implementations of superior approaches are limited to narrow window sizes unsuitable for artifact removal. Implementing the improved algorithms for our window sizes and offloading work to the GPU are both possible approaches.

Second, the excessive memory copies during the reconstruction step. While reconstruction algorithms like gridrec are well-tuned, they still engage in unnecessary memory copies from python memory structures into C-based memory structures. Changes to the reconstruction call to make the python shared memory directly available to embedded C code without excess data copies should address the memory issues associated with the reconstruction process.

Objectives (3) and (4) are in progress. Noise issues associated with the Argonne scans due to a mixture of high scan energy (imperfect for PTA) and sample quality issues have proved somewhat challenging and additional approaches such the use of unsupervised Machine Learning approaches like Noise2Noise are under examination.

REFERENCES

1. Yifu Ding, Daniel J Vanselow, Maksim A Yakovlev, Spencer R Katz, Alex Y Lin, Darin P Clark, Phillip Vargas, Xuying Xin, Jean E Copper, Victor A Canfield, Khai C Ang, Yuxin Wang, Xianghui Xiao, Francesco De Carlo, Damian B van Rossum, Patrick La Riviere, Keith C Cheng (2019) Computational 3D histological phenotyping of whole zebrafish by X-ray histotomography eLife 8:e44898
2. Lin AY, Ding Y, Vanselow DJ, Katz SR, Yakovlev MA, Clark DP, Mandrell D, Copper JE, van Rossum DB, Cheng KC. Rigid Embedding of Fixed and Stained, Whole, Millimeter-Scale Specimens for Section-free 3D Histology by Micro-Computed Tomography. J Vis Exp. 2018 Oct 17;(140):58293.
3. Gürsoy D, De Carlo F, Xiao X, and Jacobsen C. Tomopy: a framework for the analysis of synchrotron tomographic data. *Journal of Synchrotron Radiation*, 21(5):1188–1193, 2014.
4. Paganin D, Mayo SC, Gureyev TE, Miller PR, and Wilkins SW. Simultaneous phase and amplitude extraction from a single defocused image of a homogeneous object. *Journal of Microscopy*, 206(1):33–40, 2002.
5. Vo N, and Atwood RC, and Drakopoulos M. Superior techniques for eliminating ring artifacts in x-ray micro-tomography. *Optics Express*, 26(22):28396–28412, 2018.
6. Nghia T. Vo - *NSLS-II, Brookhaven National Lab, USA*; *Diamond Light Source, UK.*

ACKNOWLEDGEMENTS

The authors are very grateful to Dr. Alan Kastengren at 7BM and to Alex Deriy, Dr. Viktor Nikitin, Pavel Shevchenko, and Dr. Francesco de Carlo at 2BM of the Argonne National Laboratory Advanced Photon Source and Dula Parkinson of the Lawrence Berkeley National Laborities for their crucial assistance in temporarily integrating our detector with their hutches, data acquisition, and other intellectual contributions to the performed work. Dr. Steve Y Wang of Mobile Imaging Innovations, Inc provided essential work on the design and development of the detector hardware and Dr. Patrick J. La Riviere of the University of Chicago provided key guidance.

Enhancing Micro-CT Scanning Efficiency with Machine Learning Methods

Amogh Subbakrishna Adishesha[1], Daniel J. Vanselow[2,3], Patrick La Riviere[4], Keith Cheng [2,3,5], and Sharon Xiaolei Huang[1]

[1]College of Information Sciences and Technology, Pennsylvania State University, University Park, PA 16802
[2]Department of Pathology, Penn State College of Medicine, Hershey, PA 17033
[3]The Jake Gittlen Laboratories for Cancer Research, Penn State College of Medicine, Hershey, PA 17033
[4]Department of Radiology, The University of Chicago, Chicago, IL 60637
[5]Institute for Computational and Data Sciences, Pennsylvania State University, University Park, PA 16802

Whole-organism micro-CT captured at sub-micron resolution is vital to answering important biomedical research questions involving anatomy, microanatomy, physiology, and phenotypes induced by environmental and genetic variables. Achieving wide-field, high-resolution images with minimal artifact remains a bottleneck in this endeavor due to limitations in achieving high signal to noise and scanning efficiency. We propose a set of machine-learning based pipelines to increase the throughput of the scanning setup as well as to improve scan quality. Scanning time can be significantly reduced through sparse angular sampling during scan acquisition and/or by reducing exposure time per view. We address the challenges presented by artifacts caused by angular under-sampling or by low-photon count through a novel algorithm that is designed to understand noise distributions, super-resolution artifacts, and regional inconsistencies.

Utilizing scans of 5-day old zebrafish at Argonne National Laboratory at 0.7 µm resolution, we propose a super-resolution model that is capable of converting 2x (750 angles), 4x (375 angles) and 8x (188 angles) under-sampled data back to high quality full resolution sinogram data (1501 angles). We leverage regional attention mechanisms to maintain flat intensities across regions without subject and low noise across regions with subject. The improvements were particularly notable and important in the removal of reconstruction artifacts whose feature sizes overlapped with biological structures. Our proposed network achieves an average increase in peak signal to noise ratio (PSNR) of 27.12dB and a structural similarity index (SSIM) of 0.21, for 8x super resolution compared to the Bicubic interpolated inputs.

Enhancing Micro-CT Scanning Efficiency with Machine Learning Methods

PennState

Amogh Subbakrishna Adishesha, Daniel J Vanselow, Patrick La Riviere, Keith C. Cheng, Sharon X Huang

PennState College of Medicine

ABSTRACT

Whole-organism micro-CT captured at sub-micron resolution is vital to answering important biomedical research questions involving anatomy, microanatomy, physiology, and phenotypes induced by environmental and genetic variables. Achieving wide-field, high-resolution images with minimal artifact remains a bottleneck in this endeavor due to limitations in achieving high signal to noise, and scanning efficiency. We propose a novel machine-learning based pipeline to increase the throughput of the scanning setup as well as to improve scan quality. Scanning time can be significantly reduced through sparse angular sampling during scan acquisition and/or by reducing exposure time per view. We address the challenges presented by artifacts caused by angular under-sampling or by low-photon count through a novel algorithm that is designed to understand noise distributions, super-resolution artifacts, and regional inconsistencies.

Utilizing scans of 5-day old zebrafish at Argonne National Laboratory at 0.7 µm resolution, we propose a super-resolution algorithm that is capable of converting 2x (750 angles), 4x (375 angles) and 8x (188 angles) under-sampled data back to high quality full resolution sinogram data (1501 angles). We leverage regional attention mechanisms to maintain flat intensities across regions without subject and low noise across regions with subject. The improvements were particularly notable and important in the removal of reconstruction artifacts whose feature sizes overlapped with biological structures. Our proposed deep-learning-based algorithm achieves an average increase in peak signal to noise ratio (PSNR) of 27.12dB and a structural similarity index (SSIM) of 0.21, for 8x super resolution compared to the Bicubic interpolated inputs.

DATA ACQUISTION

The subject for the micro-CT image acquisition is placed on rotating stage in between the source and the scintillator. The subject is then rotated and angular increments to acquire projections across the 180° space. The per sample scan acquisition at 0.7 µm resolution for the Zebrafish takes about 10 minutes not accounting for the overhead and additional scanning for each sample. There is significant overlapping information between the consecutive projections and scanning efficiency can be improved through increasing the angular increment between projection and thus reducing scan time.

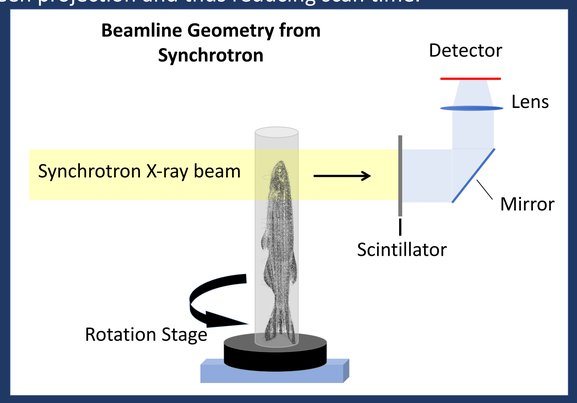

The raw projections are gain corrected and converted to sinograms of size 1500x2048 from which alternate rows are deleted to obtain the 2x under-sampled (750x2048) input. Further deletion of alternate rows leads to 4x (375x2048) and 8x (187x2048) under-sampled signals. An 8x under-sampled signal only requires 75 seconds for acquisition. In order to maintain a symmetric neural network, we up-sample the 2x,4x and 8x scans using bicubic interpolation to obtain the original size (1500x2048). However, there are significant interpolation artifacts which are illustrated in the data section.

DATA

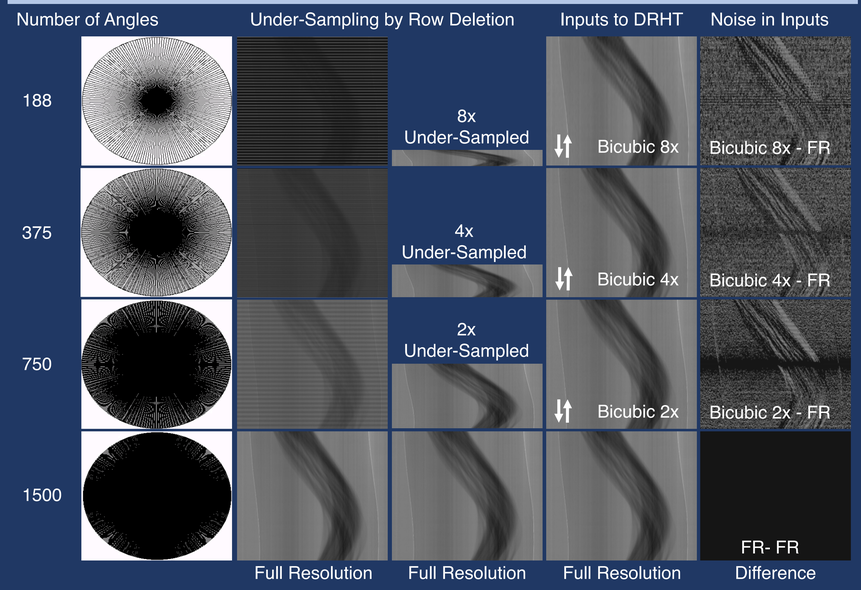

In this image, ⇅ indicates that the scan has been under-sampled and then up-sampled using bicubic interpolation. The bicubic interpolated scans have noise which increases with the scale of under-sampling. An interesting observation is that when under-sampling sinograms, we notice less sparsity near the axis of rotation while more sparsity away from the axis.

MODEL

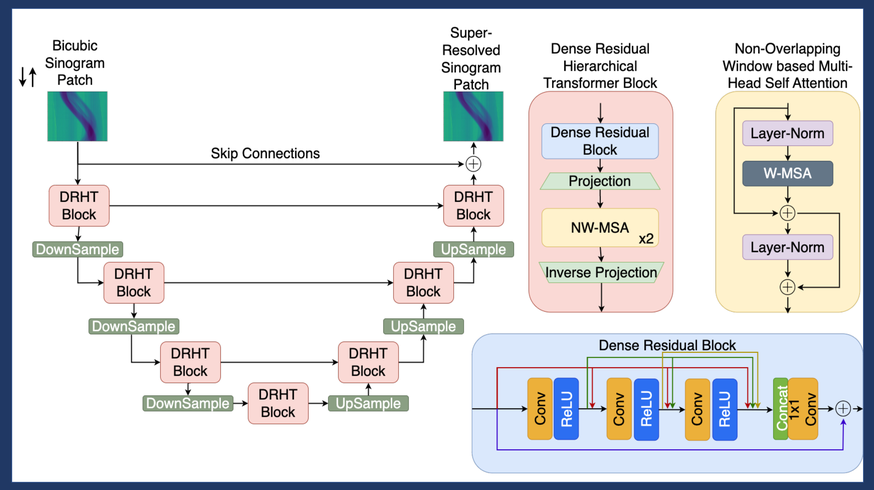

We have developed a novel deep neural network that combines three unique elements- (1) A U shaped structure to perform symmetric down-sampling and up-sampling of features, (2) Window based transformer blocks for efficient extraction of long-range feature interactions and (3) A residual network to focus on local context of the image. The three component have individually shown remarkable improvements in terms of signal to noise ratio (SNR) and structural similarity (SSIM). The network is trained over 65K samples and validated over 16K samples where each sample is of size 128x128.

RESULTS

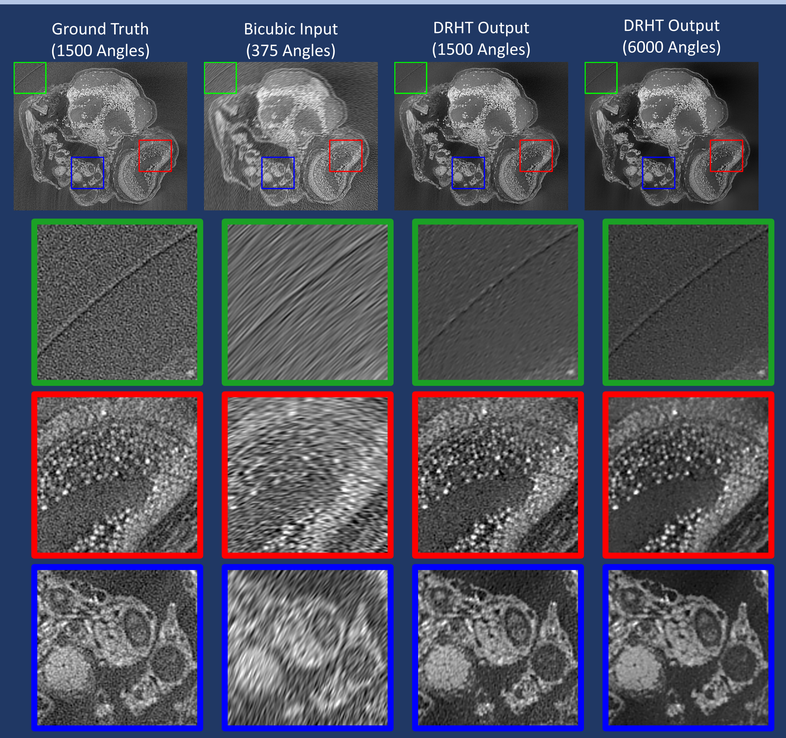

PSNR Comparison

Region	Original 1500 Angles	Bicubic 375 Angles	DRHT SR 1500 Angles
Plastic (Flat)	100	15.18	29.90
Eye Nuclei (Dense)	100	16.21	33.14
Cellular Region	100	16.66	31.71

CONCLUSION

We have proposed a robust machine learning pipeline to increase scanning efficiency by reducing the sampling rate of micro-CT projections in the angular space. The increase in efficiency leads to faster scan acquisition as well as a reduction in drift errors that usually build up over time in traditional scan acquisition settings. Additionally, we have had significant improvement in both qualitative and quantitative measures of the resulting scan.

CONTACT

Amogh Subbakrishna Adishesha
413- EBIH, College of Information Science and Technology,
aus79@psu.edu

Nanodiamond-based Anti-HIV Drug Delivery Towards the Brain

Ebenezer Owusu[1], Arkajyoti Paul[1], Deepa Roy[1], Shizue Mito[2], Upal Roy[1], and Elena A. Rozhkova[3]

[1]Department of Health and Biomedical Sciences, University of Texas Rio Grande Valley, Brownsville, TX 78520
[2]Department of Molecular Medicine, University of Texas Rio Grande Valley, Edinburg, TX 78539
[3]Center for Nanoscale Materials, Argonne National Laboratory, Lemont, IL 60439

In accordance with the statistics of the WHO in 2021, 38.4 million people were infected with HIV globally.[1] Out of this number, 36.7 million were adults and the remaining were children under 15 years. The current combination of antiretroviral therapy (cART) has changed the fatal pandemic HIV disease to a chronic disease and improved HIV related pathologies.[2] Although cART is a steppingstone in the reduction of viral load and replication in HIV patients, there is a stampede in its delivery to reservoirs such as the central nervous system (CNS) due to infective transmigration of the drug *via* the Blood Brain Barrier (BBB).[3] Recent advancement in nanomedicine-based drug delivery has been a major research topic and innovative systems for drug delivery.[4] Among nanomaterials, nanodiamonds (NDs) have become a subject of active research due to their natural biocompatibility and non-toxicity which makes them a preferable and efficient nano-carrier compared to other carbon-based materials.[5] In view of these, we used unmodified nanodiamond due to its ability to load anti-HIV drugs across the BBB as previous studies have shown its ability and efficacy to load these drugs.[2] We hypothesized that macrophages containing nanodiamonds can transmigrate through the tight junction of the BBB and release the drug into the brain and subsequently engulfed by the resident microglial cells within the brain.[6] To further advance ND-based cART, we aim to use fluorescent nanodiamonds, FND, which will have a size in the range of 50-70 nm, surface modified to attach biological molecules, higher colloidal stability, and tunable zeta potential as a multifunction traceable specifically targeting nanodrug platform.

[1] Alhaddad, A., Duran, H., Kanninen, L., & Yliperttula, M. (2020). Nanodiamonds as carriers for targeted drug delivery. Molecules, 25(22), 5375. doi: 10.3390/*molecules*25225375.
[2] Cysique LA, Brew BJ. Neuropsychological functioning and antiretroviral treatment in HIV/AIDS: a review. Neuropsychol Rev. 2009 Jun;19(2):169-85. doi: 10.1007/s11065-009-9092-3. Epub 2009 May 9. PMID: 19424802.
[3] Roy U, Drozd V, Durygin A, Rodriguez J, Barber P, Atluri V, Liu X, Voss TG, Saxena S, Nair M. Characterization of Nanodiamond-based anti-HIV drug Delivery to the Brain. *Sci Rep.* 2018 Jan 25;8(1):1603. doi: 10.1038/s41598-017-16703-9. PMID: 29371638; PMCID: PMC5785470.
[4] World Health Organization. (2020). Global HIV & AIDS statistics — 2020 fact sheet. Retrieved from https://www.who.int/news-room/fact-sheets/detail/hiv-aids (03/30/2023).
[5] Zhang L, Gu FX, Chan JM, Wang AZ, Langer RS, Farokhzad OC. Nanoparticles in medicine: therapeutic applications and developments. Clin Pharmacol Ther. 2008 May;83(5):761-9. doi: 10.1038/sj.clpt.6100400. *Epub* 2007 Oct 24. PMID: 17957183.

[6] Flannagan RS, Jaumouillé V, Grinstein S. The cell biology of phagocytosis. Annu Rev Pathol. 2012;7:61-98. doi: 10.1146/annurev-pathol-011811-132445. *Epub* 2011 Sep 9. PMID: 21910624.

Work performed at the Center for Nanoscale Materials, a U.S. Department of Energy Office of Science User Facility, was supported by the U.S. DOE, Office of Basic Energy Sciences, under Contract No. DE-AC02-06CH11357 and NIH R151R15NS108815.

Nanodiamond Based Anti-HIV Drug Delivery Towards the Brain

Ebenezer Owusu[1] Arkajyoti Paul[1], Deepa Roy[1], Shizue Mito[2], Upal Roy[1], Elena A. Rozhkova[3].

[1]Department of Health and Biomedical Sciences, University of Texas Rio Grande Valley, Brownsville, TX.

[2]Department of Molecular Medicine, University of Texas Rio Grande Valley, Edinburg., TX.

[3]Center for Nanoscale Materials, Argonne National Laboratory, Argonne, IL.

ABSTRACT

In accordance with the statistics of the WHO in 2021, 38.4 million people were infected with HIV globally [1]. Out of this number, 36.7 million were adults and the remaining were children under 15 years. The current combination of antiretroviral therapy (cART) has changed the fatal pandemic HIV disease to a chronic disease and improved HIV related pathologies [2]. Although cART is a steppingstone in the reduction of viral load and replication in HIV patients, there is a stampede in its delivery to reservoirs such as the central nervous system (CNS) due to infective transmigration of the drug *via* the Blood Brain Barrier (BBB) [3]. Recent advancement in nanomedicine-based drug delivery has been a major research topic and innovative systems for drug delivery [4]. Among nanomaterials, nanodiamonds (NDs) have become a subject of active research due to their natural biocompatibility and non-toxicity which makes them a preferable and efficient nano-carrier compared to other carbon-based materials [5]. In view of these, we used unmodified nanodiamond due to its ability to load anti-HIV drugs across the BBB as previous studies have shown its ability and efficacy to load these drugs [2]. We hypothesized that macrophages containing nanodiamonds can transmigrate through the tight junction of the BBB and release the drug into the brain and subsequently engulfed by the resident microglial cells within the brain [6]. To further advance ND-based cART, we aim to use fluorescent nanodiamonds, FND, which will have a size in the range of 50-70 nm, surface modified to attach biological molecules, higher colloidal stability, and tunable zeta potential as a multifunction traceable specifically targeting nanodrug platform.

INTRODUCTION

- According to WHO in 2021, 38.4 million people were infected with HIV globally.
- 36.7 million were adults and the remaining were children under 15 years.
- Combination antiretroviral therapy (cART) has changed HIV disease to a chronic disease and improved HIV related pathologies.
- nanodiamonds (NDs) have become a subject of active research due to their natural biocompatibility and non-toxicity.
- Inability of anti-HIV drugs to transmigrate the BBB.

MATERIALS AND METHODS

- Chemical characterization (DLS) was done to check the polydispersity index (PDI) and the sizes of FND.
- HMC-3 (CRL-3304 from ATCC) treated with various sizes and concentrations of fluorescent nanodiamond (FND) (50nm; 0.01mg/ml, 0.1mg/ml and 1.0mg/ml. same concentrations were used for 70nm and 100nm respectively for 24 hours and subsequently **ROS** and **MTT** assays were performed to observe the production of reactive oxygen species.
- One-way ANOVA was used to analyze the parametric and nonparametric variable model, Bonferroni method was used to analyze multiple comparisons test GraphPad Prism software version 8.2.0.

RESULTS

SAMPLE	SIZE	PDI
50NM	173.13±1.12	0.22± 0.01
70NM	174.83 ± 1.35	0.1 ± 0.01
DTG+AB+ND	3054.33 ± 450.42	0.65 ± 0.46
FTC+AB+ND	2392.67 ± 410.96	0.66 ± 0.06
TNT+AB+ND	3995 ± 814	0.69 ± 0.37

Table1. Dynamic Light Scattering of FND and conjugated drug (CD) in DMSO

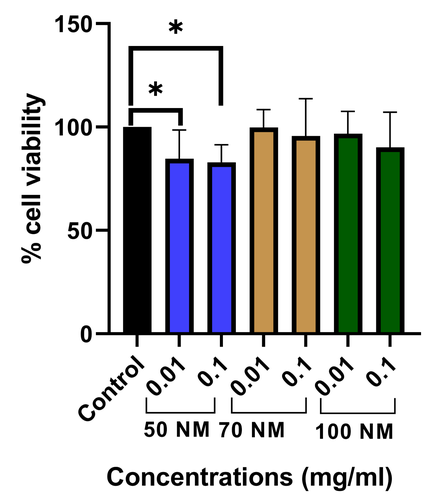

Fig 1: Cytotoxicity of HMC-3 cells treated with various concentrations of FND *p* value **= 0.003, * =0.0008**

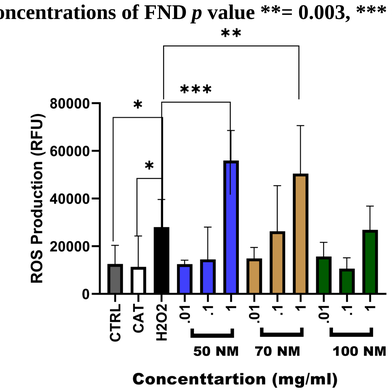

Fig 3: Oxidative response of HMC-3 cells treated with FND *p* value *= 0.0336, *=0.0159, **= 0.0233, * =0.0002**

RESULTS CONT'D

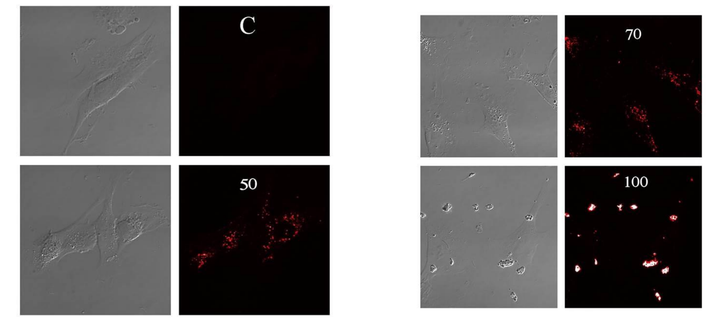

Fig 3. Immunocytochemistry of cellular uptake of FND by HMC-3cells.

- The DLS data shows that all the formulations were within the range of both the size and PDI
- From the MTT assay the 50 NM FND was toxic to the HMC-3 Cells
- The ROS assay also proved that that the highest concentrations of 50NM and 70Nm caused higher oxidative stress.
- 100NM FND showed a better cell uptake as compared to 50NM and 70NM FND

DISCUSSION

- Ant-HIV drug delivery to the brain reservoirs such as the microglia remains a challenge due to the inability of clinically available drugs to transmigrate through the BBB.
- Nanodiamond anti-HIV drug delivery to the brain serves as the means to transmigrate anti-HIV drugs through the BBB into the brain.

conclusion

- From the ROS and MTT assays, we realized that 50NM was more toxic to the cells.
- Further experiments and characterizations will be done to select the more desirable formulation between 70NM and 100NM as both did not show toxicity on the cells

ACKNOWLEDGEMENTS

- The research work is supported by NIH-Grant no. 1R01AI147731-01A1, 1R15NS108815-01, AD-RCMR at UTRGV.
- Work performed at the Center for Nanoscale Materials, a U.S. Department of Energy Office of Science User Facility, was supported by the U.S. DOE, Office of Basic Energy Sciences, under Contract No. DE-AC02-06CH11357

REFERENCES

- Alhaddad *et al.* 20202
- Cysique *et al.* 2009 PMID: 19424802
- Roy et al. 2018 PMCID: PMC5785470.
- Zhang et al. 2008. PMID: 17957183.
- Flannagan et al. 2012. PMID: 21910624.

Convenient Confinement: Examining Ion and Water Behavior near Graphene and Graphene Oxide Thin Films

Amanda J. Carr[1], Seung Eun Lee[1], Sang Soo Lee[1], Ahmet Uysal[1]

[1]Chemical Sciences and Engineering Division, Argonne National Laboratory, IL 60439

Understanding ion distributions and water orientation near graphene and graphene oxide surfaces is relevant to a range of applications, including capacitive deionization, heavy metal separations, and improved membrane performance. In each of these applications, ions and water interact with a graphene or graphene oxide surface in the small region forming between the solid and bulk liquid. Properties in this confined region greatly differ from typical bulk attributes, but experimentally probing interfaces is challenging, as most techniques are dominated by bulk signal. We experimentally characterize ion and water organization near both graphene and graphene oxide interfaces with molecular-scale resolution using a combination of surface-sensitive x-ray scattering and spectroscopy techniques uniquely available to the Advanced Photon Source. From these methods, we can fully describe the interface, including the structure of the graphene and graphene oxide films themselves, ion adsorption, and water orientation. These studies reveal the fundamental science underpinning downstream separation success.

This material is based upon work supported by the U.S. Department of Energy, Office of Science, Office of Basic Energy Sciences, Separation Science, Early Career Research Program under contract DE-AC02- 06CH11357.

CONVENIENT CONFINEMENT: EXAMINING ION AND WATER BEHAVIOR NEAR GRAPHENE AND GRAPHENE OXIDE THIN FILMS

Fundamental studies of solid/liquid and air/liquid interfaces

Amanda J. Carr, Seung Eun Lee, Sang Soo Lee, Ahmet Uysal
Chemical Sciences and Engineering Division, Argonne National Laboratory, Lemont, IL

carraj@anl.gov
@amandajcarrphd
LinkedIn.com/in/Amanda-J-Carr/

ISOLATING LANTHANIDES: CRITICAL MATERIALS

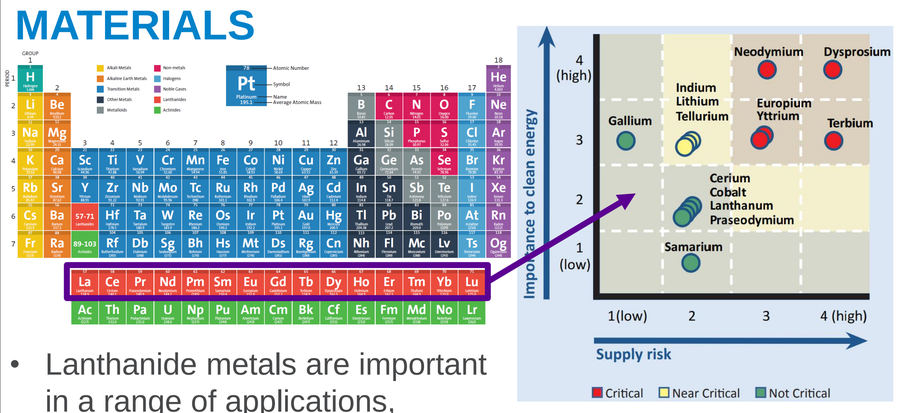

- Lanthanide metals are important in a range of applications, including optoelectronics, medical imaging, and clean energy
- Separating targeted lanthanides from complex mixtures is challenging because they are of similar size and charge
- *Need to understand basic science of lanthanide interactions, especially near interfaces*

acs.org; DOE Medium Term Outlooks: 2015–2025; windsystemsmag.com

USING 2D MATERIALS FOR SEPARATIONS

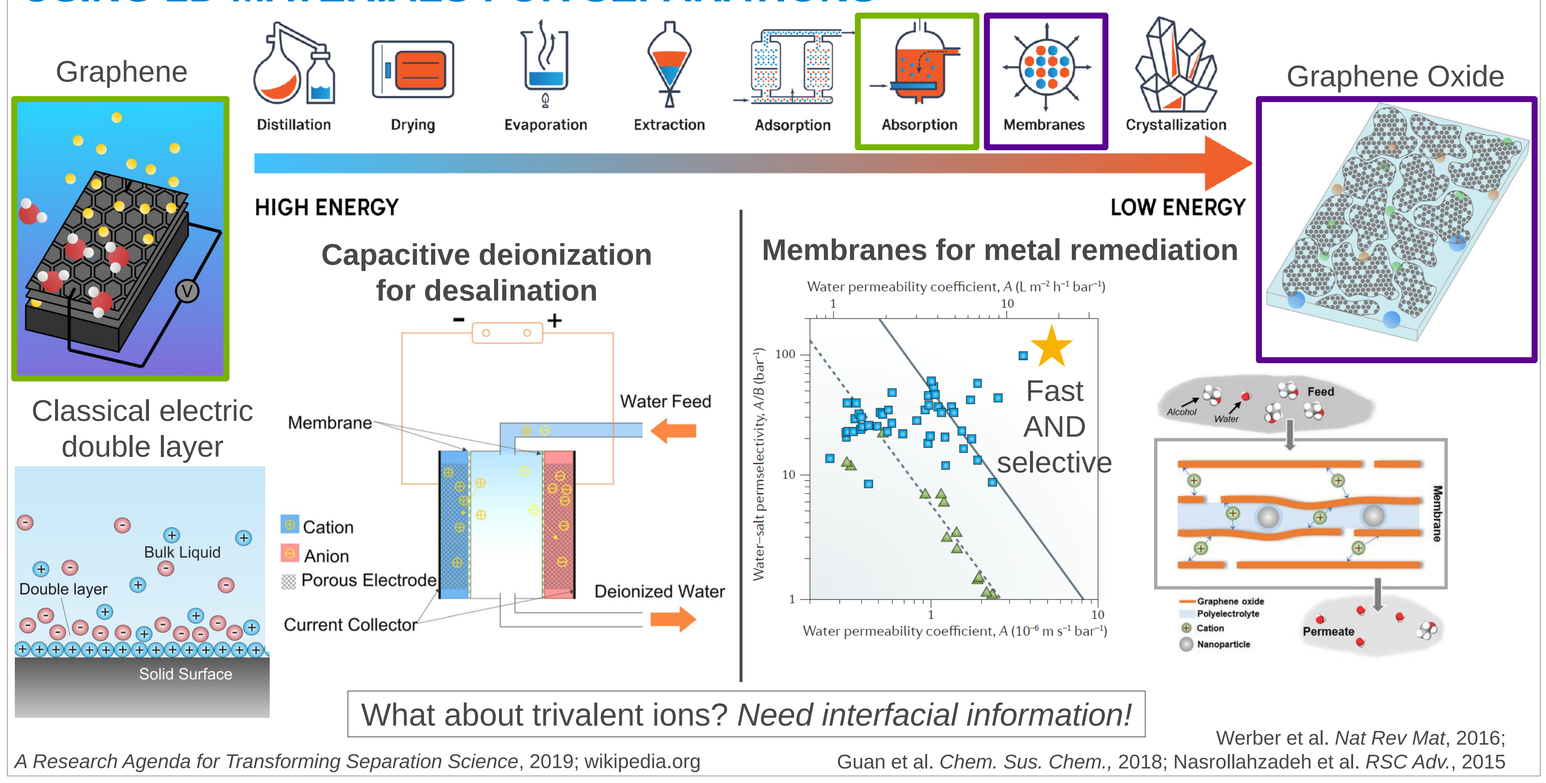

A Research Agenda for Transforming Separation Science, 2019; wikipedia.org

Werber et al. *Nat Rev Mat*, 2016; Guan et al. *Chem. Sus. Chem.*, 2018; Nasrollahzadeh et al. *RSC Adv.*, 2015

INTERFACIAL X-RAY SCATTERING AND SPECTROSCOPY

Understanding trivalent adsorption at the electrified graphene/liquid interface

High resolution x-ray reflectivity

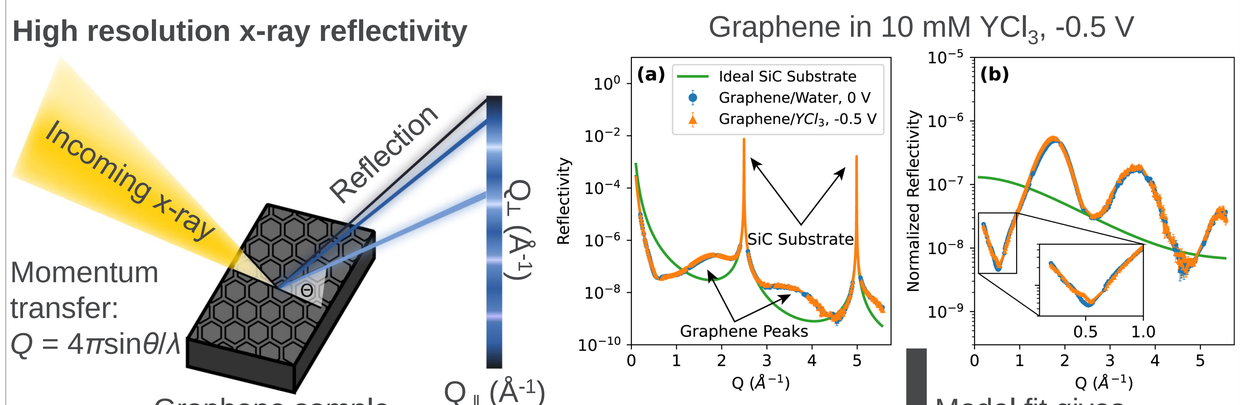

Model fit gives total electron density

Resonant anomalous x-ray reflectivity

$$f(q,E) = f^{o}(q) + f'_{R}(E) + i f''_{R}(E)$$

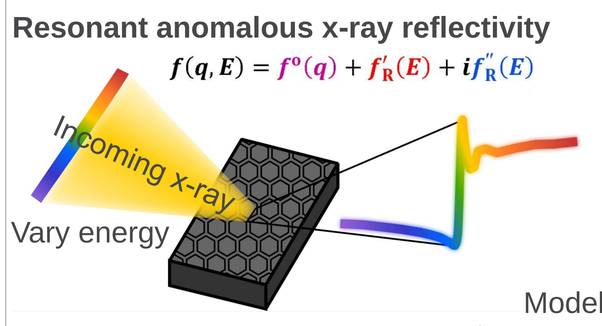

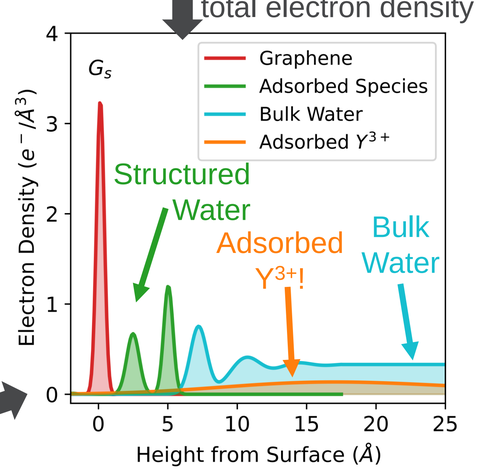

Y absorption edge

Model fit gives Y^{3+} electron density

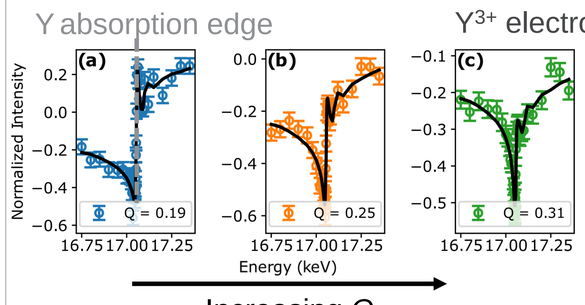

- Y retains hydration shell during adsorption
- Y overcharges graphene!

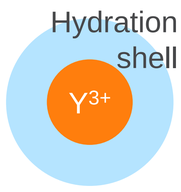

Carr et al. *J. Phys.: Condens. Matter*, 2022

Probing ion and water organization at the graphene oxide/liquid interface

Interfacial x-ray fluorescence

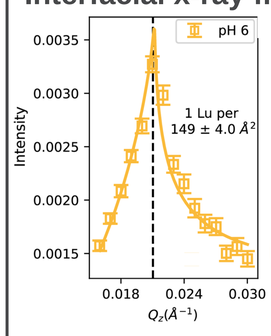

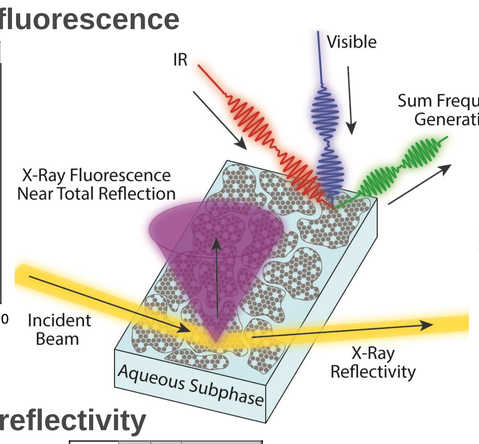

Interfacial vibrational spectroscopy

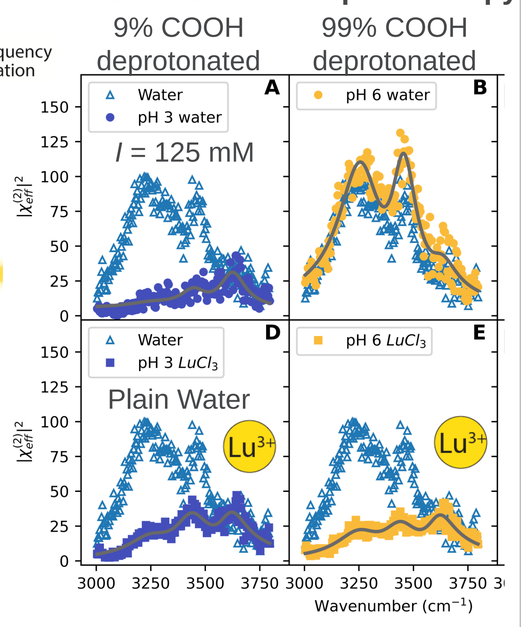

X-ray reflectivity

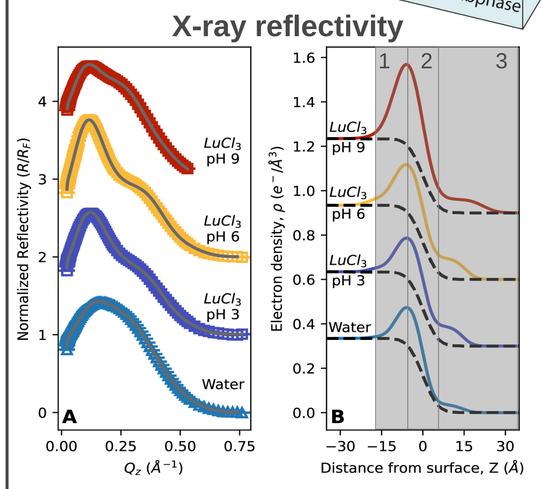

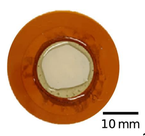

Graphene oxide membrane performance

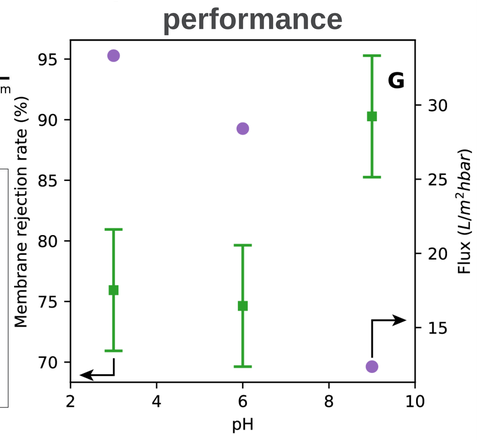

Interlayer Spacing

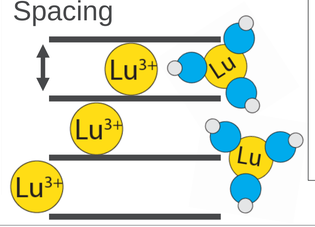

- Subphase pH affects water and ion structure at the liquid surface
- Interfacial interactions correlate to application performance

Carr et al. *ACS Appl. Mater. Interfaces*, 2022

CONCLUSIONS AND OUTLOOK

- Isolating and concentrating lanthanides from complex mixtures is challenging because they are of similar size and charge yet behave differently in classic extraction techniques
- *Need to understand basic science of lanthanide interactions, especially near interfaces*
- Surface-sensitive x-ray scattering reveal trivalent ion overcharging at the solid/liquid interface
- Non-linear spectroscopy and x-ray scattering at the air/liquid interface show variation in ion behavior depending on subphase pH, which is linked to actual membrane performance

REFERENCES

- National Academies of Sciences, Engineering, and Medicine. *A Research Agenda for Transforming Separation Science*, Washington, DC: The National Academies Press, 2019
- Werber et al. *Nature Reviews Materials*, 1, 2016
- Guan et al. *ChemSusChem*, 11, 2018
- Nasrollahzadeh et al. *RSC Advances*, 5, 2015
- Carr et al. *Journal of Physics: Condensed Matter*, 34, 2022
- Carr. *Nature Reviews Physics*, 4, 2022
- Carr et al. *ACS Applied Materials & Interfaces*, 14, 2022

ACKNOWLEDGEMENTS

This material is based upon work supported by the U.S. Department of Energy, Office of Science, Office of Basic Energy Sciences, Separation Science, Early Career Research Program under contract DE-AC02- 06CH11357. Use of the Advanced Photon Source, an Office of Science User Facility operated for the U.S. Department of Energy (DOE) Office of Science by Argonne National Laboratory, and Sectors 15-ID-C and 33-ID-D are supported by the U.S. DOE under Contract No. DE-AC02-06CH11357. NSF's ChemMatCARS Sector 15 is supported by the Divisions of Chemistry (CHE) and Materials Research (DMR), National Science Foundation, under grant number NSF/CHE-1834750.

Determining the Charge Transfer Properties of Metal-coordinated Coumarin Dyes Using X-ray and Optical Transient Absorption Spectroscopies

Danielle J. Jacoby[1], Cali Antolini[1], Abby E. Civiello[1], Christopher J. Otolski[2], Gilles Doumy[2], Anne Marie March[2], and Dugan Hayes[1]

[1]Department of Chemistry, University of Rhode Island, Kingston, RI 02881
[2]Chemical Sciences and Engineering Division, Argonne National Laboratory, Lemont, IL 60439

Organic dyes present a promising alternative to the more expensive ruthenium and iridium complexes commonly used in photoredox reactions. Ideally, such a framework should offer facile tunability of the excited state redox potential while maintaining sufficiently long excited state lifetimes for intermolecular charge transfer. Here we have augmented the coumarin derivative 4-methylesculetin with dipicolylamine to form a tetrahedral binding pocket that can then coordinate different divalent first-row transition metals, allowing us to tune the excited state redox potential by simply adding a salt. Using x-ray transient absorption spectroscopy, we have observed photoinduced reductive shifts in the K-edge spectra of the corresponding complexes of Mn^{2+} through Zn^{2+} that are consistent with the varying degrees of intramolecular charge transfer to the metals predicted by density functional theory calculations. We have also combined these x-ray measurements with optical transient absorption spectroscopy to characterize the relaxation dynamics of these complexes on timescales ranging from 100s of femtoseconds to 10s of microseconds. As expected, the Zn^{2+} complex exhibits little to no charge transfer character, and any electronic or nuclear rearrangement at the metal site fully relax within the temporal resolution of our measurement. On the other hand, all other metal complexes exhibit long-lived charge transfer states that persist for 100s of nanoseconds. Notably, the relaxation dynamics of the Co^{2+} complex include an additional time component of approximately 10 nanoseconds that is entirely absent in the other metal complexes.

Determining the Charge Transfer Properties of Metal-Coordinated Coumarin Dyes

Danielle J. Jacoby[1], Cali Antolini[1], Abby E. Civiello[1], Christopher J. Otolski[2], Gilles Doumy[2], Anne Marie March[2], and Dugan Hayes[1]*

[1]University of Rhode Island, Kingston, RI

[2]Chemical Sciences and Engineering Division, Argonne National Laboratory, Lemont, IL

4ME-Co

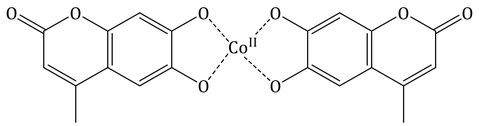

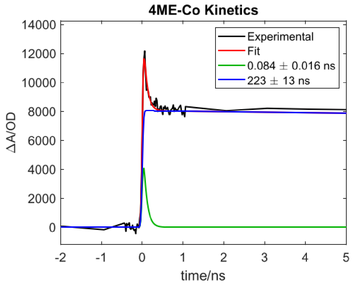

X-ray transient absorption (XTA) kinetics of 4ME-Co complex

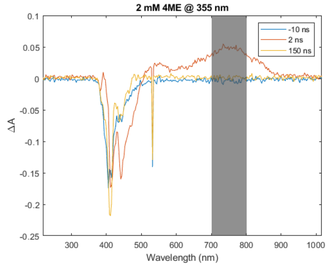

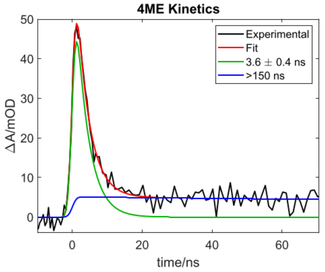

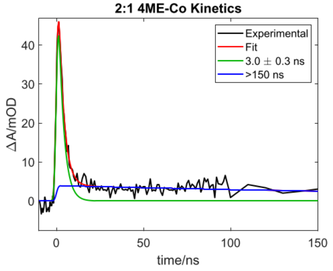

Optical transient absorption (OTA) spectra of 4ME complex at different delay times and kinetic traces of 4ME-Co averaged across 700-800 nm

Abstract

Organic dyes present a promising alternative to the more expensive ruthenium and iridium complexes commonly used in photoredox reactions. Ideally, such a framework should offer facile tunability of the excited state redox potential while maintaining sufficiently long excited state lifetimes for intermolecular charge transfer. Here we have augmented the coumarin derivative 4-methylesculetin with dipicolylamine to form a tetrahedral binding pocket that can then coordinate different divalent first-row transition metals, allowing us to tune the excited state redox potential by simply adding a salt. Using X-ray transient absorption spectroscopy, we have observed photoinduced reductive shifts in the K-edge spectra of the corresponding complexes of Mn^{2+} through Zn^{2+} that are consistent with the varying degrees of intramolecular charge transfer to the metals predicted by density functional theory calculations. We have also combined these X-ray measurements with optical transient absorption spectroscopy to characterize the relaxation dynamics of these complexes on timescales ranging from 100s of femtoseconds to 10s of microseconds.

Overview

- Promising preliminary results in using modified coumarin dyes as photoredox catalysts
- Dye exhibits short-lived* charge transfer state
- Co^{2+} exhibits long-lived ligand field states

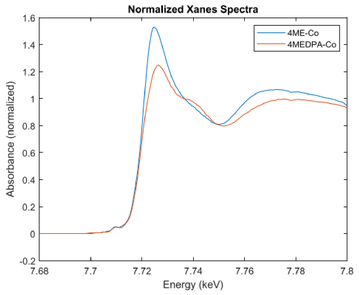

X-ray absorbance near-edge structure (XANES) spectra for 4ME-Co (blue) and 4MEDPA-Co (red) complexes

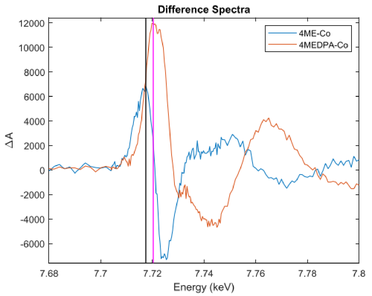

X-ray transient absorption (XTA) difference spectra for 4ME-Co (blue) and 4MEDPA-Co (red) complexes with peak difference signal highlighted

4MEDPA-Co

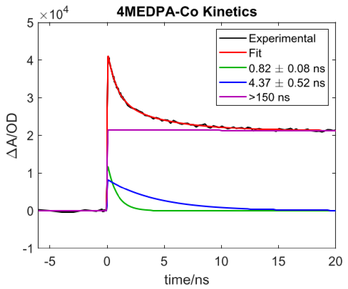

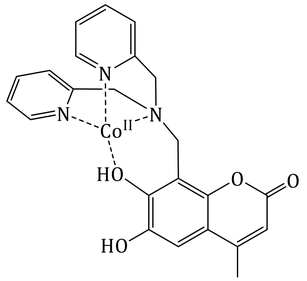

XTA kinetics of 4MEDPA-Co complex

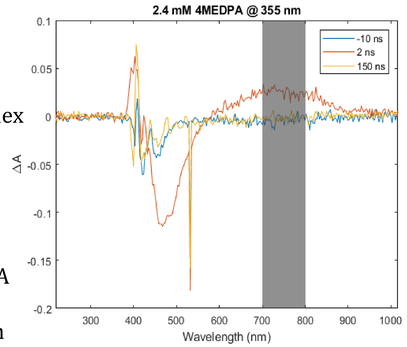

OTA spectra of 4MEDPA complex at different delay times

OTA kinetic traces of 4MEDPA and 4MEDPA-Co complexes averaged across 700-800 nm

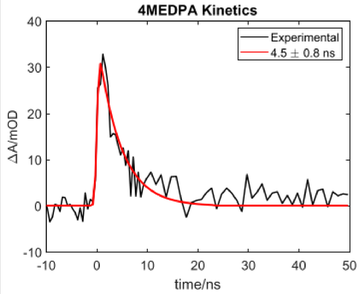

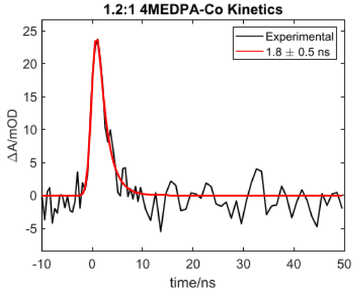

Acknowledgements

This material is based upon work supported by the U. S. Department of Energy, Office of Science, Office of Basic Energy Sciences, under Award DE-SC0019429. This research used resources (beamlines 7-ID-D and 11-ID-D) of the Advanced Photon Source, a U. S. Department of Energy (DOE) Office of Science User Facility operated for the DOE Office of Science by Argonne National Laboratory under Contract No. DE-AC02-06CH11357.

Understanding Interfaces in Rare Earth Separations via Multiple Surface Specific Probes

Ahmet Uysal[1]

[1]Chemical Sciences and Engineering Division, Argonne National Laboratory, Lemont, IL 60439

Chemical separations are central to our energy, environment, and security needs. From efficient refinery and recycling of rare earths to cleanup of contaminated underground waters, chemical separations cover a wide range of processes such as liquid-liquid extraction (LLE), membranes, and sorbents. A common theme in most processes is that the target ions need to adsorb on or go through an interface. Understanding aqueous interfaces at molecular scale, require special experimental techniques that can distinguish the interfacial structures from the overwhelmingly larger bulk.

Surface sensitive synchrotron x-ray scattering and fluorescence, and vibrational sum frequency generation (SFG) spectroscopy techniques are among the most advanced tools available to study aqueous interfaces. This poster summarizes our group's efforts in understanding aqueous interfaces in chemical separations, by combining these two experimental techniques. It demonstrates specific examples where a single method is not enough to decipher the complex interactions at the interface. The examples cover ion-amphiphile interactions in LLE and ion adsorption on graphene-oxide thin films.

The work presented here was supported by the U.S. Department of Energy, Office of Basic Energy Science, Division of Chemical Sciences, Geosciences, and Biosciences, Separation Science Program and Early Career Research Program under contract DE-AC02-06CH11357.

Manipulating Spin Anisotropy in Artificial Superlattices of Iridate with J_{eff} = 1/2 Square Lattices

Dongliang Gong[1] and Jian Liu[1]

Department of Physics and Astronomy, University of Tennessee, Knoxville, TN 37996

Spin anisotropy is a crucial factor in determining the magnetic phases of quantum materials. The competition between different symmetries of anisotropy can lead to the emergence of new states, and integrating them in one system could provide an alternative approach to achieve exotic magnetic phases. Typically, uniaxial or epitaxy strain is used to induce anisotropy in bulk or thin-film materials. In this study, we have engineered the layered structure of iridate superlattices to manipulate the spin anisotropy of Jeff = 1/2 square lattices. Specifically, we have integrated single-layer and bilayer Jeff = 1/2 square lattices in one superlattice structure as they exhibit XY-anisotropy and c-axis anisotropy, respectively. Through synchrotron x-ray diffraction, resonant x-ray magnetic scattering, magnetization, and resistivity measurements, we have discovered that the new hybrid superlattice stabilizes a unique state that differs from the single-layer and bilayer magnetic anisotropic systems. The entire hybrid superlattice orders simultaneously via a single antiferromagnetic transition at temperatures similar to the bilayer system, but with all the Jeff = 1/2 moments mainly pointing in the ab-plane, similar to the single-layer system. These findings demonstrate that combining different magnetic anisotropic systems with orthogonal properties in close proximity is a powerful approach to achieving a distinct state in the system.

Manipulating spin anisotropy in artificial superlattices of iridate with J_{eff} = 1/2 square lattice

Dongliang Gong , Junyi Yang, Lin Hao , Jian Liu
Department of Physics, University of Tennessee, Knoxville
dgong1@utk.edu

Background and Overview

Spin anisotropy is a crucial factor in determining the magnetic phases of quantum materials. The competition between different symmetries of anisotropy can lead to the emergence of new states, and integrating them in one system could provide an alternative approach to achieve exotic magnetic phases. Single-layer and bilayer J_{eff} = 1/2 square lattices are well-known examples where the presence of the extra layer turns the XY anisotropy to the c-axis anisotropy. We report on experimental realization of a hybrid SrIrO3/SrTiO3 superlattice that integrates monolayer and bilayer square lattices in one layered structure (Fig 1 (a)). By synchrotron x-ray diffraction, resonant x-ray magnetic scattering, magnetization, and resistivity measurements, we found that the hybrid superlattice exhibits properties that are distinct from both the single-layer and bilayer systems and cannot be explained by a simple addition of them. In particular, the entire hybrid superlattice orders simultaneously through a single antiferromagnetic transition at temperatures similar to the bilayer system but with all the J_{eff} = 1/2 moments mainly pointing in the ab plane similar to the single-layer system. The results show that bringing monolayer and bilayer with orthogonal properties in proximity to each other in a hybrid superlattice structure is a powerful way to stabilize a unique state not obtainable in a uniform structure.

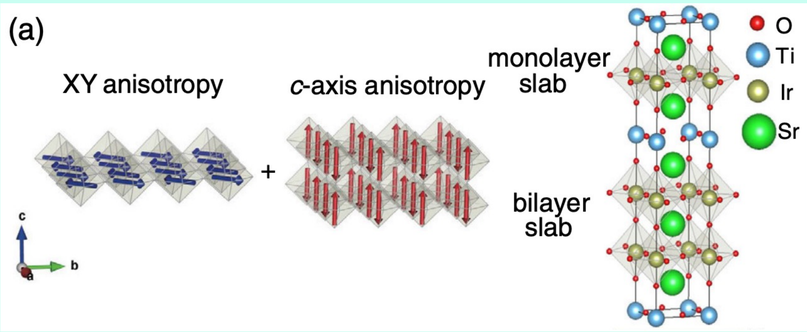

Transport measurement

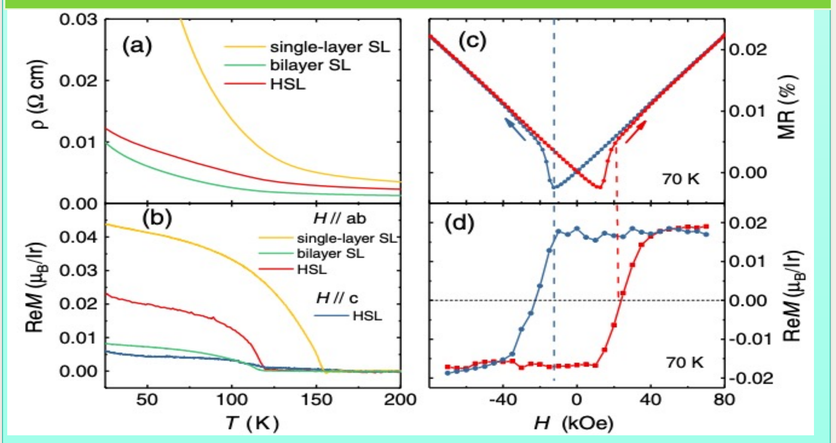

a. T_N (HSL) = 120 K, which is close to the 21 SL.
b. Single hysteresis loop suggests monolayer and bilayer has same response to the magnetic field.
c. c- axis canted moments indicates in-plane moments.

Structural characterization

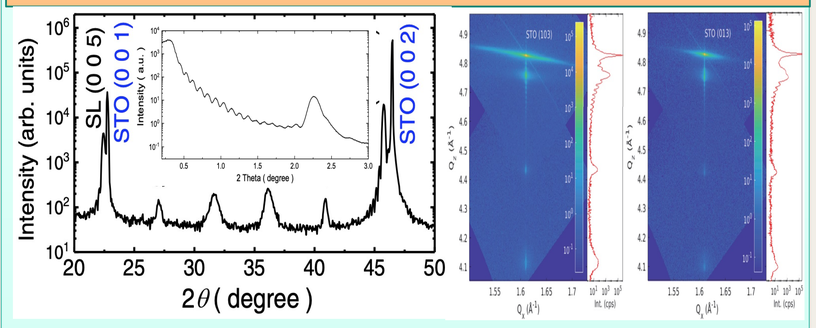

a. Five SL peaks indicates 1121 superstructure.
b. RSM confirms a fully strained state

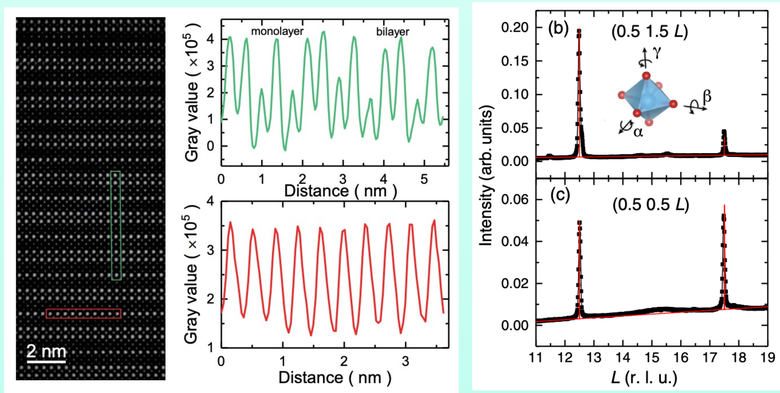

TEM results confirm the alternating stacking of monolayer and bilayer structures.

$$I = A\frac{L}{sin(\eta)}|F_N(\mathbf{Q})^2|$$

The simulation results suggest octahedral has 9° rotation angle and 4° tilt angle.

$$F_N(\mathbf{Q}) = f(\mathbf{Q})\sum_{i=1}^{n} e^{i\mathbf{Q}\cdot\mathbf{d}_i}e^{-W_i}$$

Possible Magnetic structures

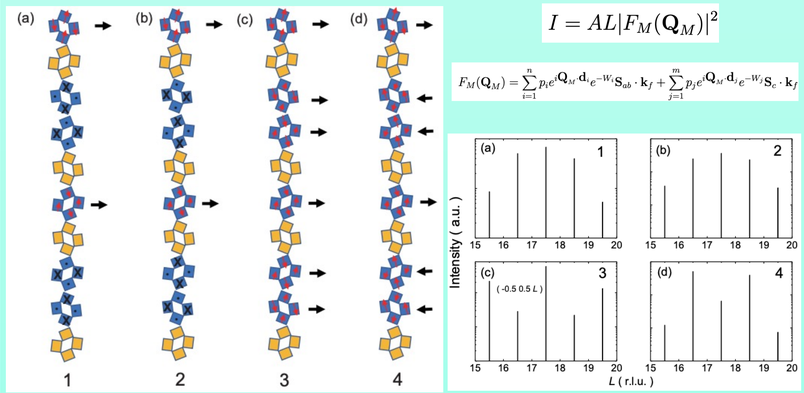

$$I = AL|F_M(\mathbf{Q}_M)|^2$$

$$F_M(\mathbf{Q}_M) = \sum_{i=1}^{n} p_i e^{i\mathbf{Q}_M\cdot\mathbf{d}_i}e^{-W_i}\mathbf{S}_{ab}\cdot\mathbf{k}_f + \sum_{j=1}^{m} p_j e^{i\mathbf{Q}_M\cdot\mathbf{d}_j}e^{-W_j}\mathbf{S}_c\cdot\mathbf{k}_f$$

Four possible magnetic structured can describe the transport results, and could produce half-integer peaks in diffraction pattern. But they have different intensity modulations. Thus, they can be distinguished by magnetic scattering.

Resonant elastic x-ray scattering

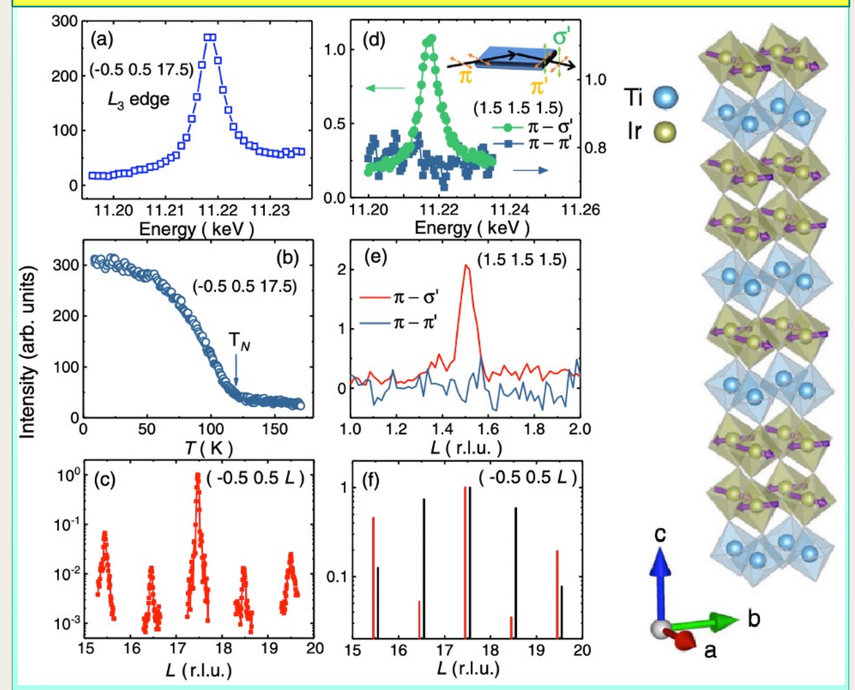

The experimental diffraction pattern in (c) is consistent with the magnetic structure (c) as shown at the right side.

The in-plane moment were confirmed by polarization dependence of incoming beam and analyzed beam in horizontal geometry (d) and azimuthal dependence in vertical geometry.

Summary

In conclusion, we have engineered a HSL that combines single-layer and bilayer Jeff = 1/2 square lattices which are known to have orthogonal anisotropy individually. Our systematic study shows that the HSL has an a−a−c− octahedral pattern and hosts a nearly planar canted AFM order through a single transition below 120 K. Compared to the single-layer and the bilayer SLs, the HSL stabilizes a new distinct state that cannot be described by the simple addition of the monolayer and bilayer properties since the proximity forces them to couple with each other electronically and magnetically. The results show that bringing monolayer and bilayer 2D systems with orthogonal properties close to each other in a hybrid superlattice structure is a powerful way to obtain unique states that cannot be achieved in a uniform structure, opening a way to search for new quantum states in layered materials.

Acknowledgement

Jian Liu acknowledges support from the National Science Foundation under Grant No. DMR-1848269. Junyi Yang acknowledges funding from the State of Tennessee and Tennessee Higher Education Commission (THEC) through their support of the Center for Materials Processing. Lin Hao acknowledges support from the National Natural Science Foundation of China (Grant No. 12104460) and the High Magnetic Field Laboratory of Anhui Province.

THE UNIVERSITY OF TENNESSEE KNOXVILLE

INSTITUTE FOR ADVANCED MATERIALS & MANUFACTURING

U.S. DEPARTMENT OF ENERGY

DARPA Defense Advanced Research Projects Agency

Origin of Chirality in Transition-metal Dichalcogenides

Hyun-Woo. J. Kim[1, 2], Kwangrae Kim[1], Seunghyeok Ha[1], Hoon Kim[1], Jin-Kwang Kim[1], Jaehwon Kim[1], Hyunsung Kim[1], Junyoung Kwon[1], Saegyeol Jung[3, 4], Changyoung Kim[3, 4], Ayman Said[2], and B. J. Kim[1*]

[1]Department of Physics, Pohang University of Science and Technology, Pohang 37673, South Korea
[2]Advanced Photon Source, Argonne National Laboratory, Lemont, IL 60439
[3]Center for Correlated Electron Systems, Institute for Basic Science, Seoul 08826, South Korea
[4]Department of Physics and Astronomy, Seoul National University, Seoul 08826, South Korea

1T-TiSe2, an archetypal charge density wave (CDW) system with a 2×2×2 unit cell below T_C=200K,[1] is proposed to exhibit chirality at T*=180K by various experiments such as photogalvanic effect,[2] transport and specific heat measurements,[3] but the mechanism how chiral symmetry is broken remains poorly understood. In this talk, we will discuss our measurements using Raman spectroscopy, x-ray diffraction and inelastic x-ray scattering (IXS). We show that chiral symmetry in the lattice sector is already broken at the T_C and therefore that a second order transition at T* is absent. Our IXS data show no anomaly of phonons at the zone center of the 2×2×2 unit. Instead, we observe splitting of Eg phonon modes measured by Raman spectroscopy, and a forbidden reflection by x-ray diffraction, which indicate breaking of the chiral symmetry. Our results show that chirality in the CDW phase arises from mutually incompatible symmetry properties of charge density modulations and atomic displacements, transforming as a continuous scalar field and a vector field on a discrete lattice, respectively.

Inelastic X-ray experiment performed at 30-ID was supported by Ayman Said was performed by Hyun-Woo. J. Kim.

[1] M. Holt et al., Phys. Rev. Lett. 86, 3799 (2001)
[2] Su-Yang et al., Phys. Rev. Lett. 86, 3799 (2020)
[3] John-Paul Castellan et al., Phys. Rev. Lett. 110, 196404 (2013)

Strain tunable emergent magnetic state in Sr_2IrO_4

Shashi Pandey[1]

[1]University of Tennessee, Knoxville, TN 37996

Iridates are one of the extensively studied transitional metal oxides because of the unique combination of the electron-electron and spin-orbit interaction. Sr_2IrO_4 is a notable example, which is a quasi-two-dimensional J_{eff} =1/2 canted antiferromagnetic (AF) Mott insulator with a layered structure that is remarkably similar to the parent phase of weakly spin-orbit-coupled high-Tc cuprates. However, due to the built-in spin-orbit entanglement, the J_{eff} = 1/2 moments can form significant inter-site quadrupoles in contrast to the S=1/2 moments of Cu ions. The resulting magnetoelastic coupling leads to spontaneous tetragonal symmetry breaking by the AF order in the B1g channel. In the experiment, we compared the elasto-responses of the AF order to *in-situ* B1g and B2g strains representing two orthogonal symmetry configurations. While the B1g strain efficiently detwins the spontaneous AF domains, new states that break the translational symmetry along the c-axis emerge with the B2g strain [1]. Our model analysis shows that such an emergent state is driven by an unusual quartic interaction of B2g symmetry, competing with the intrinsic B1g anisotropy, and can be *in situ* tuned by the applied strain.

[1] S. Pandey et. al., Controllable Emergent Spatial Spin Modulation in Sr2IrO4 by *In Situ* Shear Strain, Phys. Rev. Lett. 129, 027203 (2022).

Emergence of a new magnetic state in Sr_2IrO_4 induced by an *in situ* B_{2g} strain

Shashi Pandey, Han Zhang, Junyi Yang, Dongliang Gong, Chengkun Xing, Alexander Sizemore, Weiliang Yao, Haidong Zhou and Jian Liu
Department of Physics & Astronomy, University of Tennessee, Knoxville, Tennessee, 37996

IAMM Institute for Advanced Material and Manufacturing

Overview

Spatially modulated phases, where the order parameter varies over multiple structural building blocks, widely exist in nature from physical systems to biological systems. Exotic spin textures are the magnetic version of this kind with prominent examples including various forms of spin spirals and magnetic skyrmions, which have been extensively studied for magnetoelectric effects, topology, spintronics, etc.

Motivation

Competition of anisotropic interactions of different symmetry channels could be an attractive alternative mechanism for stabilizing spatially modulated phases because rotational/mirror symmetry-breaking is a much more common character of magnetic ordering

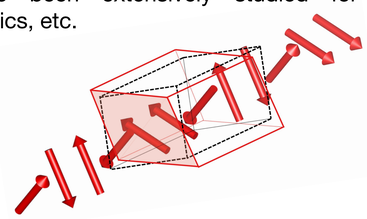

Figure. A 12-IrO_2-plane magnetic modulation with a broken translational symmetry induced by a B2g strain

Here, we demonstrate that competing anisotropy of B_{1g} and B_{2g} symmetry leads to a magnetic modulation consisting of 12 IrO_2 planes in Sr_2IrO_4.

5d Iridate System

A unique competition between the strong Spin Orbit Coupling (SOC) and electron correlation yields the Jeff = ½ Mott Insulating State in 5d Iridate system.

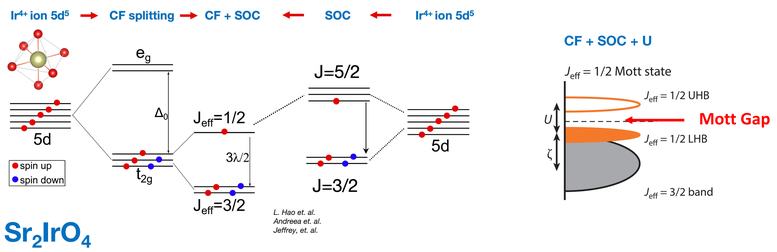

Sr_2IrO_4

Single layered perovskite with a tetragonal crystal structure

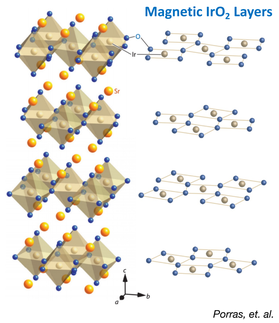

Octahedral Rotation

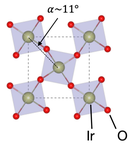

introduces a non-zero net moment in each Ir layer.

Metamagentic (MM) Transition

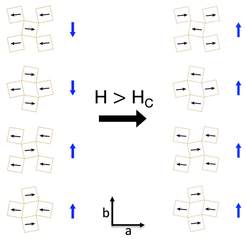

Hamiltonian for Magnetic Interactions

$$H = H_s + H_{s-l}$$

$$H_s = J\vec{S}_i \cdot \vec{S}_j + J_z S_i^z S_j^z + \vec{D} \cdot [\vec{S}_i \times \vec{S}_j] + K(\vec{S}_i \cdot \vec{r}_{ij})(\vec{S}_j \cdot \vec{r}_{ij})$$

$$H_{s-l} = \tilde{g}_1 \varepsilon_1 \left(s_i^x s_j^y + s_i^y s_j^x\right) + \tilde{g}_2 \varepsilon_2 \left(s_i^x s_j^y - s_i^y s_j^x\right)$$

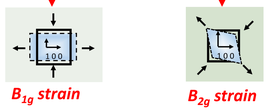

By virtue of the **pseudo-JT effect**, the lattice distortion is coupled linearly with the spin quadrupoles.

Controlling the pseudo-JT Effect?

Yes, apply the *in-situ* strain. The magnetoelastic effect should induce the uniaxial anisotropy in the system.

Inhouse Magnetoresistance (MR)

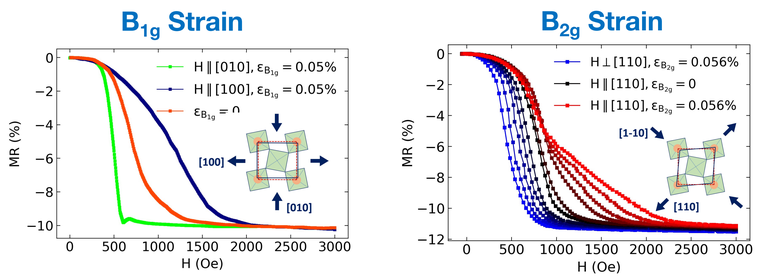

With the B_{1g} strain stretching the a-axis of the sample, the MM transition upshifts (downshifts) with $H \parallel b$ ($H \parallel a$). However, it shows a strange response with a B_{2g} strain with $H \parallel [110]$ – the emergence of a long-extended tail in MR.

XRMS measurement with *in-situ* B2g strain

In Sr_2IrO_4, the magnetic Bragg diffraction comes from scattering by Iridium t_{2g} electrons. The XRMS using the L edge (2p→5d), does the selective resonant enhancement allowing the study of the magnetic structure in this system.

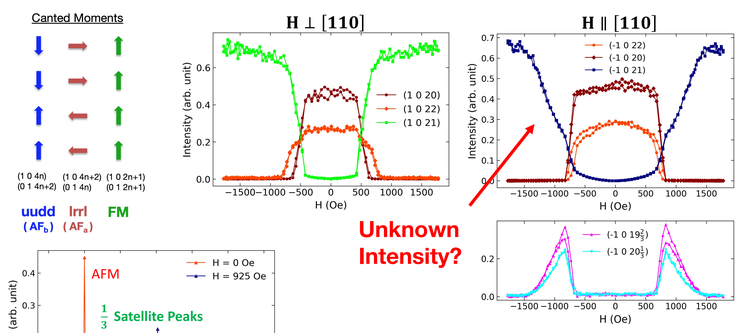

"Broken Translational Symmetry (BTS)" of the magnetic ordering with a 12-layer spin modulation along the c-axis.

The increase in the FM intensity even after the disappearance of AF intensity is coming from the expense of the 1/3 satellite peak intensity.

Minimal Free Energy Model

$$F(M_j = MS_j) = E_0 + E_H$$

$Q_j^{(1)} \equiv S_j^{a2} - S_j^{b2}$ is the B_{1g} quadrupole

$$E_0 = \delta_c \sum_j (-1)^j \left(S_j^a S_{j+1}^a - S_j^b S_{j+1}^b\right) + k_b \sum_j Q_j^{(1)2} + k_b' \sum_j Q_j^{(1)} Q_{j+1}^{(1)}$$

NN Anisotropic Interaction | Onsite Anisotropic Interaction | NN Quad-Quad Interaction

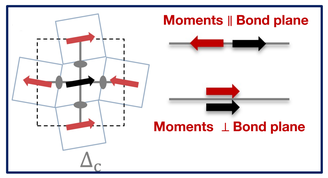

E_0 term stabilizes the ↑-↑-↓-↓ stacking pattern of the canted moments

Zeeman Energy Term

$$E_H = \boldsymbol{M}.\boldsymbol{H} = MH \sum_j \cos(\theta_j - \beta)$$

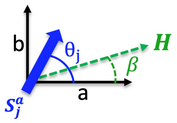

Case I : B1g Strain

$$F(M_j) = E_0 + E_H + E_{B_{1g}}$$

$$E_{B_{1g}} = \varepsilon_{B_{1g}} k_{1u} \sum_j Q_j^{(1)}$$

B1g Uniaxial Interaction

B2g Quartic Interaction

Case II : B2g Strain

$$F(M_j) = E_0 + E_H + E_{B_{2g}}$$

$$E_{B_{2g}} = \varepsilon_{B_{2g}} \kappa \sum_j S_j \cdot S_{j+1} (Q_j^{(2)} + Q_{j+1}^{(2)})$$

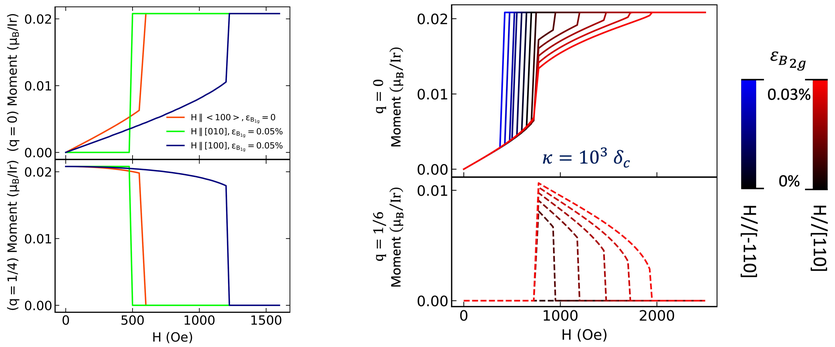

➢ A non-trivial B2g quartic interaction reproduces the observed strain effects. Also, the emergence of such interaction reveals nontrivial physics of high-order anisotropy.

Evolution and Origin of the BTS State

The q = 1/6 modulation sets in by "inserting" an unpaired moment (red) in between the adjacent pairs (blue). Both the unpaired and paired moments become fully aligned at a sufficiently large field.

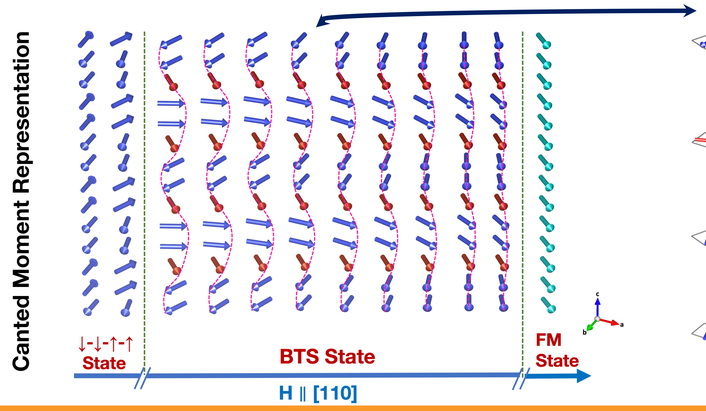

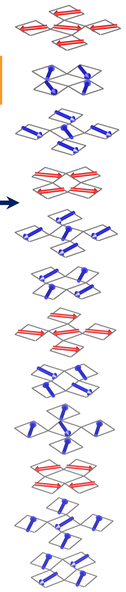

Conclusion

In a system like Sr_2IrO_4 where the magnetic ordering breaks rotational symmetry, introducing an anisotropy that is orthogonal to the spontaneous anisotropy of the system, could lead to translational symmetry-breaking resulting in the emergence of a new magnetic state. The possibility of introducing the competition between the B_{1g} and B_{2g} anisotropy in Sr_2IrO_4 by *in situ* strain allows continuous tuning of the spatial modulation. This approach to trigger competition and obtain controllable new phases could be applicable to many quasi-2D materials due to the critical role of anisotropy in stabilizing low-dimensional magnetic orders.

This work is supported by the the Organized Research Unit Program at the University of Tennessee. The in-situ strain control and measurement setup is partially supported by AFOSR DURIP Award FA9550-19-1-0180; the SARIF at the University of Tennessee and as part of Programmable Quantum Materials, an Energy Frontier Research Center funded by the U.S DOE, Office of Science, Basic Energy Sciences (BES), under award DE-SC0019443. Transport measurement was supported by the U.S. Department of Energy under grant no. DESC0020254 and the Electromagnetic Property (EMP) Lab Core Facility at the University of Tennessee. This research used resources of the Advanced Photon source; a U.S. Department of Energy (DOE) Office of Science User Facility operated for the DOE Office of Science by Argonne National Laboratory under contract no. DE-AC02-06CH11357.

Collaborators : J. Sanchez, Z. Liu, J.-H. Chu (UW, Seattle); A. F. May (ORNL); J. W. Kim, P. J. Ryan (ANL)

Single-crystal X-ray Diffraction at Extreme Conditions (GSECARS)

Stella Chariton[1] and Vitali B. Prakapenka[1]

[1]Center for Advanced Radiation Sources, University of Chicago, Chicago, IL 60637

The advantages of using single crystals over powdered samples in x-ray diffraction experiments are well known [1]. Analysis of single-crystal x-ray diffraction (SCXRD) data has traditionally allowed us to obtain explicit solutions of complex structures, detect small structural distortions, retrieve accurate displacement parameters as well as provide chemical characterization of new materials. The SCXRD method is becoming more and more appealing in the high-pressure research community nowadays [2]. It is now possible to study in great details the crystal structure, physical and chemical properties of minerals and materials, important for materials science, even in the megabar pressure range using the diamond anvil cell (DAC). Even at high pressure, where the coverage of the reciprocal space is restricted by the DAC design, SCXRD data provide more information than the one-dimensional diffraction patterns collected from powdered samples.

Here we review the sample and DAC preparations that are necessary prior to a single-crystal x-ray diffraction experiment, we describe the data collection procedures at GSECARS (sector-13), and we discuss the data processing using various software. A few examples, on carbonate minerals and various metal oxides, but also weakly scattering compounds, such as CO_2, are presented in order to demonstrate not only the challenges but also the advantages of using single crystals for solving the structures of complex high-pressure polymorphs or novel compounds, as well as to better constrain the compressibility and the high-pressure structural evolution of known compounds.

[1] P. Dera (2010) *All different flavors of synchrotron single crystal X-ray diffraction experiments.* High-Pressure Crystallography, Springer, Dordrecht, p11-22.
[2] T. Boffa-Ballaran et al. (2013) *Single-crystal X-ray diffraction at extreme conditions: a review.* High Pressure Research, 33, p453-465.

Contact: chariton@cars.uchicago.edu

Single-crystal X-ray Diffraction at Extreme Conditions (GSECARS)

Stella Chariton & Vitali B. Prakapenka

Center for Advanced Radiation Sources, The University of Chicago, Chicago, IL 60637, USA

Introduction

- ✓ Analysis of single-crystal X-ray diffraction (**SCXRD**) data has traditionally allowed us to obtain explicit solutions of complex structures, detect small structural distortions, retrieve accurate displacement parameters as well as provide chemical characterization of new materials.
- ✓ The **SCXRD** method is becoming more and more appealing in the high-pressure research community nowadays. It is now possible to study in great details the crystal structure, physical and chemical properties of minerals and materials, important for materials science, even in the Mbar pressure range using the diamond anvil cell (DAC).
- ✓ Here we review the sample and DAC preparations that are necessary prior to a **SCXRD** experiment, we describe the data collection procedures at **GSECARS** beamline (sector 13), and we discuss the data processing using various software.

What can you do using SCXRD?

- ✓ Obtain Accurate Equations of State
- ✓ Detect small structural distortions
- ✓ Study evolution of polyhedra with pressure
- ✓ Retrieve accurate displacement parameters
- ✓ Solve directly the structure of novel phases
- ✓ Determine unit cell parameters with great precision
- ✓ Provide chemical characterization of new compounds

What are your limitations ?

You will be able to perform SCXRD experiments on geomaterials and materials of great importance to material science over a broad pressure and temperature range, however…

☹ You will not be able to collect SCXRD patterns during laser-heating

☺ *BUT you can collect quick 2D-patterns during heating sessions…*

☹ Collection of low symmetry phases can be challenging at very high pressures due to the limited number of available reflections.

☺ *BUT there are a few known strategies to overcome such problems…*

13-IDD Beamline at GSECARS

MAIN CHARACTERISTICS

- ✓ X-ray energy: 6-42 keV
- ✓ X-ray beam size: 2x3 μm²
- ✓ X-ray detectors: Pilatus 1M CdTe, MARCCD, Pilatus 300K-W
- ✓ Laser system: 2 YLF, 100 W max output
- ✓ Others: Remote pressure control, cryostat & open flow cooler, multi-channel collimator, on-line ruby fluorescence, X-ray fluorescence, on-line Raman spectroscopy & more

Apply for beamtime after the APS-U!

Contact us for questions

Brief SCXRD collection Protocol

Procedure	Average time needed
1) Create calibration files.	~ 30 min
2) Place your DAC under the beam.	~ 5 min
3) Scan and locate the center of the sample chamber	Depends on the size of the sample, the pressure in the cell or other special conditions ~ 5 min
4) Perform centering procedures (i.e. find the center of rotation)	Under special conditions it can be challenging ~ 5 min
5) Collect a wide scan or a still image	… seconds
6) Evaluate your patterns, adjust exposure times, beam flux or choose another sample location if needed	~ seconds – few minutes
7) Collect a step scan	~ 2-5 min (for a standard step scan)
8) Preliminary processing of your SCXRD data before you change sample, heat or increase pressure *(recommended)*	Strongly depends on users experience, computer performance & sample complexity ~ 15 – 30 min
9) Laser-heating sessions	~ 10 – 30 min *(depends on every single case)*
10) Set a **grid collection** to map the heated sample and find the most interesting areas to collect step scans.	Depends to the size of the grid, type of scan and exposure time…

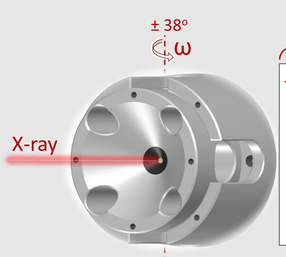

Example of a step scan → 152 frames, 1 s exposure every 0.5°

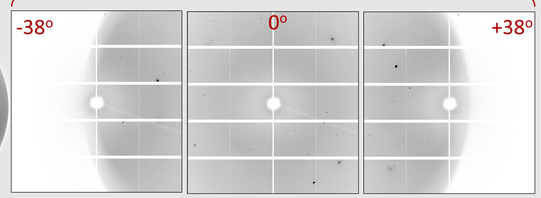

Requirements for a successful SCXRD experiment at extreme conditions

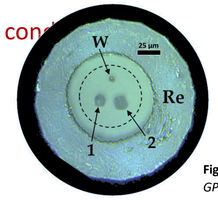

- ✓ **A diamond anvil cell with large opening angle**
- ✓ **Boehler-Almax type anvils and seats**
- ✓ **Single crystals of high-quality and appropriate size**

Figure 1: *Two $CoCO_3$ crystals and a W chip arranged in the sample chamber at 5 GPa. At high pressures the gasket hole will shrink as indicated by the dashed circle.*

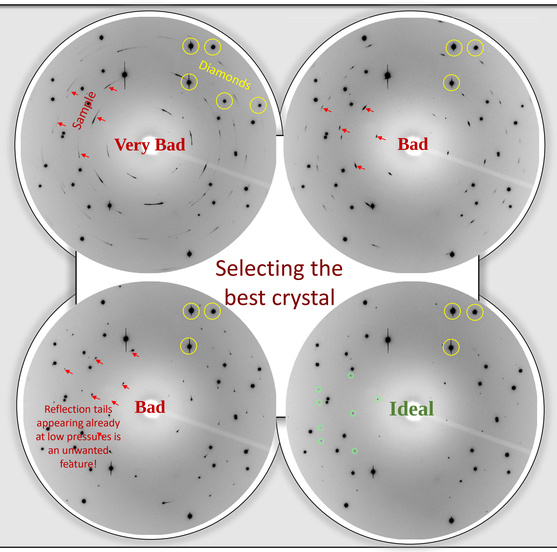

Cold compression & laser heating

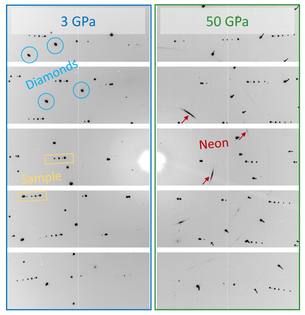

Figure 2: *An ideal single crystal of Re_2C is compressed from 3 GPa to 50 GPa at room temperature. The sample's reflections remain sharp and intense at high pressures.*

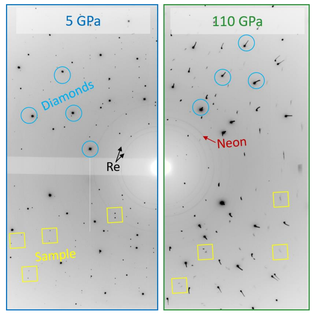

Figure 3: *An ideal single crystal of $ZnCO_3$ is compressed from 5 GPa to 110 GPa at 300 K. The crystal slowly deteriorates leading to broad and weak reflections. The data quality becomes too poor for single-crystal analysis in this case.*

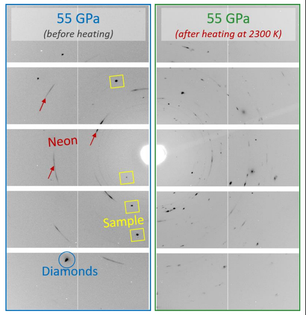

Figure 4: *An $(Fe_{0.3}Mg_{0.7})CO_3$ crystal at 55 GPa is laser heated at 2300 K for 1 min. Many new reflections appear. The sample partially dissociates in formation of high-pressure Fe_3O_4 (Bbmm).*

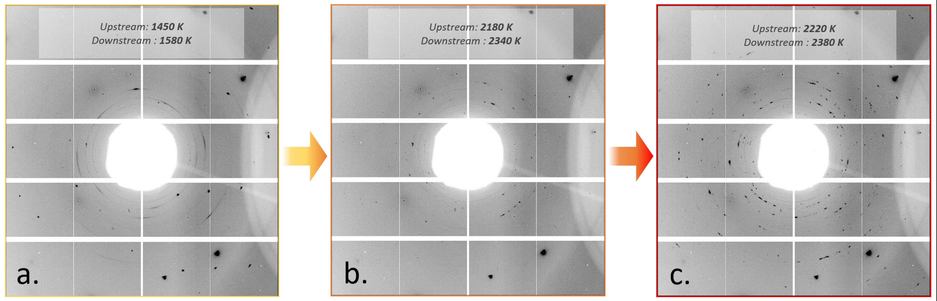

Figure 5: *X-ray diffraction patterns (still images) of an $(Fe_{0.3}Mg_{0.7})CO_3$ crystal at 55 GPa collected* **during double-sided laser heating**. ***a)*** *The carbonate crystal remains stable, the user must increase temperature.* ***b)*** *First signs of crystallization of a new phase, the user must keep the temperature stable to allow better crystal growth.* ***c)*** *The new reflections appear promising for a SCXRD collection to start, the user must quench.*

Processing single-crystal XRD data

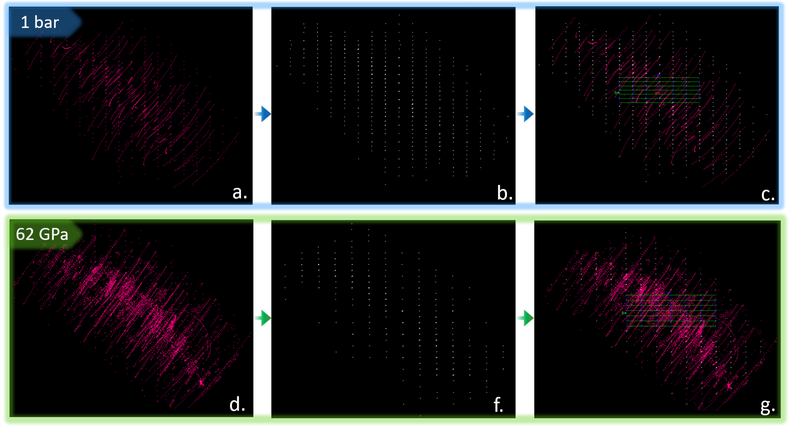

Figure 6: Reflections in the Ewald sphere using CrysAlis^{PRO}. Two datasets for $NiCO_3$ SCXRD collection in the diamond cell are depicted along the a*- axis, **a-c)** at 1 bar, and **d-f)** at 62 GPa. Starting from a and d, the user has to separate the sample reflections (**b** and **e**) from the trash-reflections arising from the high-pressure environment as shown in **c** and **f**.

Suggested software for data evaluation & processing

Dioptas : exploration of 2D – XRD patterns, data evaluation prior to SCXRD collections *(Prescher et al. 2015)*

CrysAlis^{PRO} : Single-crystal XRD data processing, determination of unit cell, integration of reflection intensities, absorption corrections *(Agilent Technologies)*

J A N A : Structure solution, refinements of atomic coordinates, site occupancies, anisotropic displacement parameters and others *(Petricek et al. 2014)*

Structure Solution

$$\rho_{xyz} = \frac{1}{V}\sum_{hkl} F_{hkl} exp[-2\pi i(hx + ky + lz)]$$

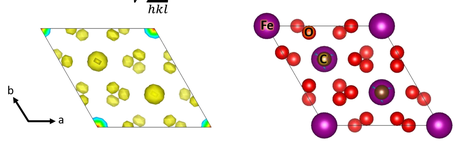

Electron density map

Atoms located

Multigrain & Multiphase analysis

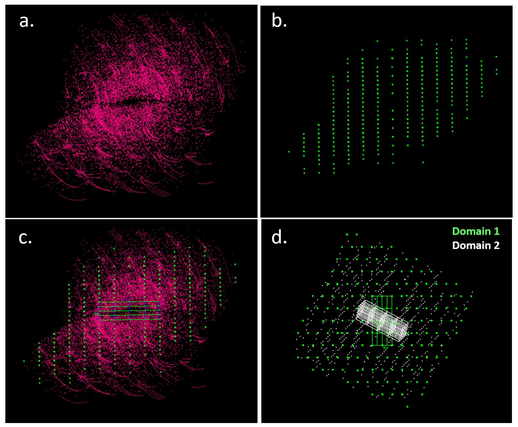

Figure 7: Reflections of a $MnCO_3$ crystal after heating in the Ewald sphere. **a)** Peaks arise from several domains and the high-pressure environment. In **b** and **c**, a $Mn_4C_4O_{13}$ domain is found and depicted along the a-axis. Many domains belong to the same phase, but have different orientations. In **d**, a second $Mn_4C_4O_{13}$ domain is found. In this dataset we found **9 domains of $Mn_4C_4O_{13}$ and 2 domains of δ-Mn_2O_3.**

Example of a single-phase multigrain sample : CO_2-V

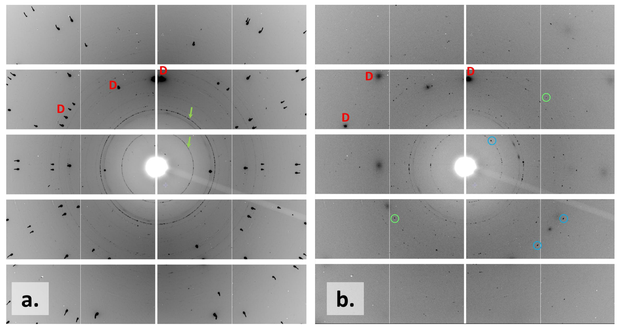

Figure 8: **a)** A wide XRD image collected while the DAC is constantly rotating from -38 to 38° for 20 sec. The CO_2-V peaks appear almost like a powder (green arrows). In reality this is a polycrystalline sample. **b)** A still XRD image collected while the DAC is stationary for 3 sec. Through the multigrain analysis we are able to separate the reflections from at least two different CO_2-V grains (green & blue circles) and process them independently.

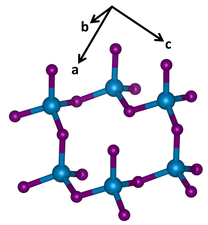

$I\bar{4}2d$, 45 GPa, ~1450 K

a= 3.568(2) , c=5.890(6)

V=74.98(8)

107 unique reflections

R1= 5.8% , wR2= 6.1%

Suggested References: Derd **(2010)** High-Pres Cryst., p11-22.; Boffa-Ballaran et al. **(2013)** High Pres Res, 33, p453-465; Chariton et al **(2020)** Acta Cryst, E76, 715-719; Bykova et al. **(2016)** Nature Com, 7, 10661; Bykov et al. **(2018)** Acta Cryst, E74, 1392-1395

Acknowledgments: This work was performed at GeoSoilEnviroCARS (The University of Chicago, Sector 13), Advanced Photon Source (APS), Argonne National Laboratory. GeoSoilEnviroCARS is supported by the National Science Foundation – Earth Sciences (EAR – 1634415) and Department of Energy- GeoSciences (DE-FG02-94ER14466). This research used resources of the Advanced Photon Source, a U.S. Department of Energy (DOE) Office of Science User Facility operated for the DOE Office of Science by Argonne National Laboratory under Contract No. DE-AC02-06CH11357.

The GM/CA@APS Structural Biology Facility Upgrade Plan

Robert F. Fischetti[1], Nagarajan Venugopalan[1], Michael Becker[1], Stephen Corcoran[1], Dale Ferguson[1], Mark Hilgart[1], David J. Kissick[1], Oleg Makarov[1], Craig M. Ogata[1], Sergey Stepanov[1], Qingping Xu[1], Shenglan Xu[1], Janet L. Smith[2].

[1]GM/CA CAT, Argonne Natl Lab, Argonne, IL
[2]Life Sciences Institute, Univ Michigan, Ann Arbor, MI

The National Institute of General Medical Sciences and National Cancer Institute Structural Biology Facility at the Advanced Photon Source (GM/CA@APS) operates a national user facility for structural biology with synchrotron beamlines specializing in intense, tunable micro-beams for crystallography. The facility includes canted-undulator beamlines, 23ID-B, and 23ID-D, that provide stable, intense X-ray beams of user-selectable size down to 5-micron, an intuitive user interface for experiment control, and an automated data processing pipeline. The beamlines have high-capacity automounters and PAD detectors (Dectris), allowing rapid data collection. GM/CA users have been very productive, resulting in almost 2000 publications and over 3350 protein data bank deposits. Our micro-crystallography developments supported the research of Brian Kobilka, who was awarded the 2012 Nobel Prize in Chemistry for studies of G-protein-coupled receptors (GPCRs).

We plan to upgrade the beamlines during the APS dark period to exploit the high brightness of the APS-U. New state-of-the-art focusing optics and endstation instrumentations will be installed. The focusing optics will be replaced with EEM-polished mirrors (JTEC) in mechanical benders (AXILON) and compound refractive lenses (CRLs) (RXOPTICS, AXILON). The mirrors could focus the full beam down to 5 microns with an intensity of over 5×10^{13} photons/sec, and with the CRL transfocator, the beam could be focused to sub-micron dimensions with an intensity greater than 1×10^{13} photons/sec at 12 keV. The new optics will provide extremely intense, clean, stable, and rapidly adjustable beam sizes between 1-30 microns. The monochromator on 23-ID-D will be modified to increase thermal and mechanical stability and raise the maximum energy to 35 keV to exploit the high intensity of the APS-U at high energy. Each endstation will be replaced, and one high-stability table will support the CRL translocator and sample environment. The new goniometer will allow data collection on crystals as small as one micron and provide rapid scanning of random or periodic fixed target samples. A Dectris Eiger2 16M CdTe detector will allow high-speed, high-efficiency X-ray detection on 23-ID-D. The new pyBluIce GUI and beamline control software will enable sophisticated data collection routines such as 3D-rastering and helical data collection, fully automated (unattended) data collection, and routine serial crystallography data collection from fixed target and injector-based sample delivery systems. These small, ultra-intense, high-energy beams will create game-changing opportunities for exciting new structural biology research.

GM/CA@APS has been funded by the National Cancer Institute (ACB-12002) and the National Institute of General Medical Sciences (AGM-12006, P30GM138396). The Eiger 16M detector was funded by an NIH-Office of Research Infrastructure Programs, High-End Instrumentation Grant (1S10OD012289-01A1).This research used resources of the Advanced Photon Source, a

U.S. Department of Energy (DOE) Office of Science User Facility operated for the DOE Office of Science by Argonne National Laboratory under Contract No. DE-AC02-06CH11357.

The GM/CA@APS Structural Biology Facility Upgrade Plan

Robert F. Fischetti[1], Nagarajan Venugopalan[1], Michael Becker[1], Stephen Corcoran[1], Dale Ferguson[1], Mark Hilgart[1], David J. Kissick[1], Oleg Makarov[1], Craig M. Ogata[1], Sergey Stepanov[1], Qingping Xu[1], Shenglan Xu[1], Janet L. Smith[2]

[1]*GM/CA@APS, X-ray Science Division, Advanced Photon Source, Argonne National Laboratory, Argonne, IL 60439, USA and* [2]Life Sciences Institute, Univ Michigan, Ann Arbor, MI

Abstract

The National Institute of General Medical Sciences and National Cancer Institute Structural Biology Facility at the Advanced Photon Source (GM/CA@APS) operates a national user facility for structural biology with synchrotron beamlines specializing in intense, tunable micro-beams for crystallography. The facility includes canted-undulator beamlines, 23ID-B, and 23ID-D, that provide stable, intense X-ray beams of user-selectable size down to 5-micron, an intuitive user interface for experiment control, and an automated data processing pipeline. The beamlines have high-capacity automounters and PAD detectors (Dectris), allowing rapid data collection. GM/CA users have been very productive, resulting in almost 2000 publications and over 3350 protein data bank deposits. Our micro-crystallography developments supported the research of Brian Kobilka, who was awarded the 2012 Nobel Prize in Chemistry for studies of G-protein-coupled receptors (GPCRs).

We plan to upgrade the beamlines during the APS dark period to exploit the high brightness of the APS-U. New state-of-the-art focusing optics and endstation instrumentations will be installed. The focusing optics will be replaced with EEM-polished mirrors (JTEC) in mechanical benders (AXILON) and compound refractive lenses (CRLs) (RXOPTICS, AXILON). The mirrors could focus the full beam down to 5 microns with an intensity of over 5×10^{13} photons/sec, and with the CRL transfocator, the beam could be focused to sub-micron dimensions with an intensity greater than 1×10^{13} photons/sec at 12 keV. The new optics will provide extremely intense, clean, stable, and rapidly adjustable beam sizes between 1-30 microns. The monochromator on 23-ID-D will be modified to increase thermal and mechanical stability and raise the maximum energy to 35 keV to exploit the high intensity of the APS-U at high energy. Each endstation will be replaced, and one high-stability table will support the CRL translocator and sample environment. The new goniometer will allow data collection on crystals as small as one micron and provide rapid scanning of random or periodic fixed target samples. A Dectris Eiger2 16M CdTe detector will allow high-speed, high-efficiency X-ray detection on 23-ID-D. The new pyBluIce GUI and beamline control software will enable sophisticated data collection routines such as 3D-rastering and helical data collection, fully automated (unattended) data collection, and routine serial crystallography data collection from fixed target and injector-based sample delivery systems. These small, ultra-intense, high-energy beams will create game-changing opportunities for exciting new structural biology research.

Upgraded optical devices – HDM, KB-mirrors, CRL and End-stations

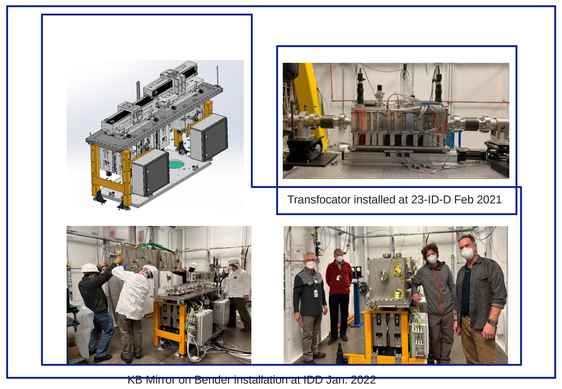

KB-1 and CRL installed in Hutch D on January 2022

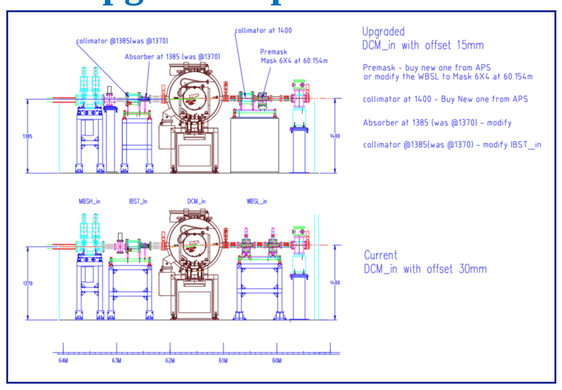

DCM offset changed from 30mm to 15 mm in Hutch C

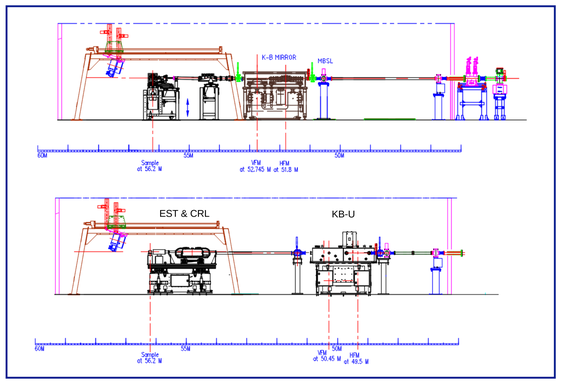

New KB mirror, Endstation and CRL-2 in Hutch B

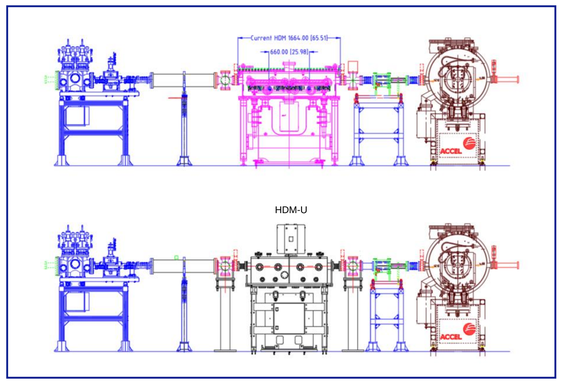

Upgraded HDM in Hutch A

CRL on ID-D station

CRL Transfocator commissioning

- Design specification
  - Provide ~1-micron focus over 5 – 35 keV using white beam slit source with APS and undulator source with APS-U
  - Center of lenses should be aligned to ~ 5 micron
  - Use multiple diameter lenses for full energy range and to minimize amount of translation 31-50μm, 131-200μm, 7–500μm
- September 2020: installed with bent V-grove rail and only ½ lenses
  - Gained experience aligning and changing configuration vs. energy (# of lenses, longitudinal shift, pitch and roll alignment)
  - Transfocator pitched with "shift" motion due to pressure from vacuum bellow. Effect reduced by shimming (Oleg Makarov)
- January 2021: new V-grove rail design installed with all 169 CLR lenses and apertures
  - Began commission minimal focal size over 5 – 35 keV energy range
- May 2021: accelerometer measurements
- Until 2022/08/20: operation condition good

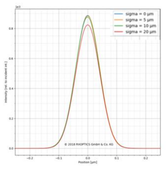

Effect of lens alignment on peak intensity and focal size

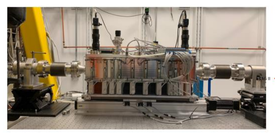

Transfocator installed in 23-ID-D

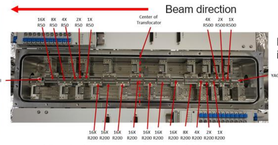

View inside the transfocator ~600mm long

Transfocator V-grove rail lens center deviation:
V1: R ± 70 micron (bent rail)
V2: R ± 6 micron
Measured by Shenglan Xu with Argonne metrology

CRL Transfocator micro-focus commissioning

WBSL	Theoretical focal size	Measure focal size
Open	15 x <1 (H X V, FWHM)	13.9 x 5.4
Closed	1.0 x 1.0	2.0 x 2.7

maging the full undulator source with CRLs
- Due to the large differences in the horizontal and vertical properties of the undulator source (size, divergence), the foci are not in the same plane (see plot)
- Design: use one or two mirrors with paraboloid lenses to adjust focal position (no linear lenses!)

Micro-focusing
- Horizontal direction: use new canted-undulator white beams slits (WBSL) to define a small source point
- Vertical direction: either image undulator source and use mirror(s) to adjust focal length or use WBSL

Challenges
- Measuring the beam size
  - Old knife edges gave broad beam profiles
  - Newly fabricated knife edges give sharper profiles
- Vertical profile was dominated by intensity feedback dither of the DCM 2nd crystal, and table vibrations
- Horizontal and vertical focal points move up to 25 mm depending on WBSL status, open or closed
- Beams size decreases linearly with WBSL size
- Discovered coupling between horizontal and vertical WBSL sizes (adjusted roll this shutdown)

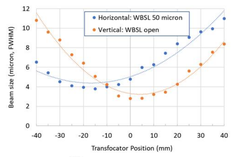

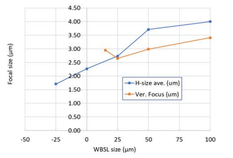

Before CRLs

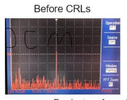

CRL focused beam

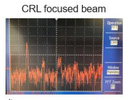

Fourier transform of Intensity

18

Argonne

KBM_in metrology

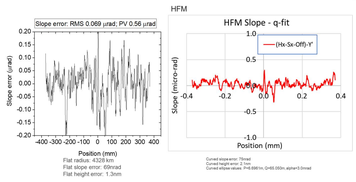

LTP metrology at the APS of the HFM mirror in the bender.

Left: the raw slope effort for the HFM when flat.
Right: the residual slope for the HFM when the mirrors is bent to the ideal curvature to image the undulator source to the sample position.

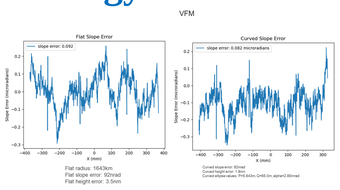

LTP metrology of the VFM mirror in the bender at the APS.
Left: the raw slope effort for the VFM when flat.
Right: the residual slope for the VFM when the mirrors is bent to the ideal curvature to image the undulator source to the sample position.

Beam properties with upgraded optics at 12 keV

APS with new mirrors and CRLs

	Full	Optimized mini-beams (mirrors)			CRLs & WBSL
Beam size (μm)	62.5 × 4.1	20	10	5	1.2 × 1.2
Intensity (ph/s)	3.5×10^{13}	7.4×10^{12}	3.6×10^{12}	2.1×10^{12}	2.3×10^{11}
Intensity gain†	1.0	5.1†	9.7†	10.0†	>100*

† Compared to ID-D 2016 values
* Compared to ID-B 2011 values

Comparison of sources with only CRL optics

	APS	APS-U Brightness	APS-U Timing
Beam size (μm)	13.3 × 0.5	0.7 × 0.3	0.6 × 0.4
Intensity (ph/s)	4.2×10^{12}	9.6×10^{12}	8.3×10^{12}
Flux density (ph/s/μm²)	8.2×10^{11}	6.4×10^{13}	3.8×10^{13}
Flux density ratio	1	78	46

*Beam size values are FWHM, H × V

Acquisition and Processing Software Upgrades

High Data Rate MX

Faster detectors with streaming and multi-image files require software changes to reach their full potential.

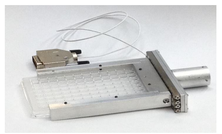

Serial Crystallography

Fixed-target sample mounts such as the one above are optimally used with new tools to plan data collection.

HTTP Queue

A queue of HTTP commands allows for future automation of any functionality including vector and raster.

Data Processing

Images will be streamed both to local computing resources and the ALCF, where a supercomputer provides more CPU cores when needed.

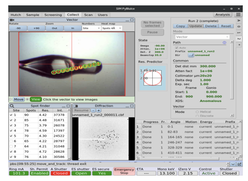

Refined UI

A rewritten acquisition UI is highly modular and ready for high-speed acquisition, complex automation and is completely scriptable for quickly adding new collect modes.

GM/CA@APS has been funded by the National Cancer Institute (ACB-12002) and the National Institute of General Medical Sciences (AGM-12006, P30GM138396). The Eiger 16M detector was funded by an NIH-Office of Research Infrastructure Programs, High-End Instrumentation Grant (1S10OD012289-01A1).This research used resources of the Advanced Photon Source, a U.S. Department of Energy (DOE) Office of Science User Facility operated for the DOE Office of Science by Argonne National Laboratory under Contract No. DE-AC02-06CH11357.

The Advanced Photon Source is funded by the U.S. Department of Energy Office of Science

Structural Basis of CEACAM1 Oligomerization

Amit K. Gandhi[1], Zhen-Yu J. Sun[2], Yu-Hwa Huang[1,4], Richard S. Blumberg[1]

[1]Division of Gastroenterology, Department of Medicine, Brigham and Women's Hospital, Harvard Medical School, 75 Francis Street, Boston, MA 02115
[2]Department of Cancer Biology, Dana-Farber Cancer Institute, Boston, MA 02215

The human (h) CEACAM1 observed to form oligomers and micro-clusters on the cell surface which are thought to regulate hCEACAM1-mediated signaling. However, the structural basis for hCEACAM1 higher-order oligomerization is currently unknown. To understand this, we report a hCEACAM1 IgV oligomer and nuclear magnetic resonance (NMR) studies predict that such oligomerization is not impeded by the presence of carbohydrate side-chain modifications. In addition, using UV spectroscopy and NMR studies, we show that oligomerization is further facilitated by the presence of a conserved metal ion (Zn^{++} or Ni^{++}) binding site on the G strand of the FG loop. Together these studies provide biophysical insights on how GFCC' and ABED face interactions together with metal ion binding may facilitate hCEACAM1 oligomerization beyond dimerization.